Normal fault damage zone growth in map view from analogue models

Sylvain Mayolle, Roger Soliva, Stéphane Dominguez, Christopher Wibberley

Journal of Structural Geology 176 (2023) 104975

Normal fault damage zone growth in map view from analogue models

Sylvain Mayolle [a, b, *], Roger Soliva [a], Stéphane Dominguez [a], Christopher Wibberley [c]

[a] *Géosciences Montpellier, Univ Montpellier, CNRS, Montpellier, France*

[b] *Universita` degli Studi di Milano - Bicocca, Dipartimento di Scienze dell'Ambiente e della Terra, Milano, Italy* [c] *TotalEnergies, CSTJF, Av. Larribau, 64018, Pau, France*

* Corresponding author. Universita` degli Studi di Milano - Bicocca, Dipartimento di Scienze dell'Ambiente e della Terra, Milano, Italy.

E-mail addresses: sylvain.mayolle@unimib.it (S. Mayolle), roger.soliva@umontpellier.fr (R. Soliva), dominguez@umontpellier.fr (S. Dominguez), christopher. wibberley@totalenergies.com (C. Wibberley).

Abstract:

Better understanding of stress perturbations, strain propagation and fluid flow in the upper crust require characterisation of fault damage zone evolution. Outcrop studies help understand the different processes operating during fault movement; but capture little about the evolution through time. In this study, we investigate damage zone evolution using high-resolution analogue modelling; simulating the growth of a normal fault population. The incremental strain reveals that early deformation stages occur by strain localisation into corridors of distributed deformation. Active deformation within these corridors becomes narrower as segment linkage occurs, leading to the formation of master faults, encouraging further localisation of incremental strain. This results in wide zones of cumulative strain around the fault, accommodated by different types of fault damage geometry, which formed at very different stages of the fault system growth. We also highlight the new concept of "fault system damage", that shows similarities with observations in nature. These first descriptions of the fault damage evolution allow an understanding of the composite content of damage zones. This gives support to assess zones of permeability enhancement in naturally fractured reservoirs, and proposes a view of damage distribution for targeting fluid flow, geothermal resources, leaks, micro/macro seismicity and mechanical properties of fault zones.

https://doi.org/10.1016/j.jsg.2023.104975 Received 27 July 2023; Received in revised form 27 September 2023; Accepted 30 September 2023. Available online 1 October 2023. 0191-8141/

1. Introduction

Fault zone structures affecting the brittle part of the crust are usually classified into two main zones, Core Zones (CZ) and Damages Zones (DZ) (e.g. Caine et al., 1996; Shipton and Cowie, 2001; Billi et al., 2003; Kim et al., 2004 Berg and Skar, 2005). Core zones are formed by intense deformation producing fault rocks with variable degrees of comminution and cementation (e.g. Sibson, 2000; Fossen, 2016). The damage zone can develop in a volume of rock by generation of several types of structures, such as fractures, folds, deformation bands, or minor secondary faults, but the primary structure of the protolith is preserved. These damage structures are formed by different processes occurring from fault initiation to maturation (Cowie and Shipton, 1998; Peacock, 2001; Peacock et al., 2017; Ostermeijer et al., 2022). However, the overall understanding of damage zone growth remains very incomplete due to the static nature of outcrop observations and their size being below the scale of resolution in 3D seismic data sets. Fault damage zones are major heterogeneities impacting fluid flow and fault mechanical behavior that must be considered for the exploration and production of economic fluids, geological storage or modelling earthquake ground motion (Faulkner et al., 2010). More precisely, the geometrical properties of DZs define the size and plumbing geometry of underground fluid conduits, and therefore significantly affect reservoir permeability, heat transfer and perturbation in geothermal systems (Taillefer et al., 2018; Milesi et al., 2019), borehole interactions, fluid/energy recovery, and strategy of borehole location in aquifer, oil and gas and energy storage fields (Solum and Huisman, 2017; Wibberley et al., 2017). Moreover, it is also very important for risk assessment studies since it defines the geometrical properties and dimension of microseismicity patterns (Goebel and Brodsky, 2018; Schmittbuhl et al., 2021), but also the properties of head waves reflected against the surrounding less damaged rock, that can lead to super-shear earthquakes (Ampuero and Mao, 2017).

The fault damage zone is defined as the deformed volume of rock around the main fault core zone of highly deformed fault rocks and slip surfaces, containing structures directly related to the development of the main fault within a protolith that remains recognisable (Caine et al., 1996; Shipton and Cowie, 2001, 2003; Berg and Skar, 2005; Schueller et al., 2013; Choi et al., 2016). Damage zones have mainly been described from map and outcrops (e.g. McGrath and Davison, 1995; Billi et al., 2003; Micarelli et al., 2003; Johansen and Fossen, 2008; Maqbool et al., 2016; Mayolle et al., 2019; Ostermeijer et al., 2020) but remain limited by the scale of observation, the dimensions of the outcrops and the description of the structures in a static state. For example, the damage thickness measurements are often scanlines, i.e. 1D datasets (e. g. Du Bernard et al., 2002; Micarelli et al., 2006; Savage and Brodsky, 2011; Schueller et al., 2013; Choi et al., 2016; Mayolle et al., 2019; Balsamo et al., 2019). The quality of the outcrops is also rarely sufficient for an exhaustive observation, more particularly for faults with large displacements and therefore large damage zones. Map data often allow a 2D analysis of fault zones, generally limited by image resolution and usually involving a single fault, and even frequently only on one side of the fault, hence not allowing identification of potential damage asymmetry for example (Berg and Skar, 2005). In previous studies, observations in the plane of fault slip (e.g. Evans, 1990; McGrath and Davison 1995; Schulz and Evans, 2000; Heermance et al., 2003; Chester et al., 2004; Kim et al., 2004; Faulkner et al., 2006; de Joussineau et al., 2007; Johansen and Fossen, 2008; Childs et al., 2009; Savage and Brodsky, 2011; Schueller et al., 2013; Perrin et al., 2016; Hansberry et al., 2021;

Ostermeijer et al., 2022) have generally been favored over out-of-plane observations (e.g. Knott et al., 1996; Beach et al., 1999; Shipton and Cowie, 2001; Maqbool et al., 2016; Balsamo et al., 2019; Martinelli et al., 2020; Silva et al., 2022). Only a few seismic data sets allow a 3D view of fault zones with low-resolution compared to outcrop observation (Liao et al., 2019; Schwarz and Krawczyk, 2020; Karam et al., 2021; Alongi et al., 2022). Previous studies also provide static observations and data sets while analogue modelling studies have illustrated the evolution of fault zones, showing that they are strongly controlled by the segmentation process (Dresen et al., 1991; Marchal et al., 1998, 2003; Mansfield and Cartwright, 2001; Bellahsen and Daniel, 2005; Schlagenhauf et al., 2008; Rotevatn et al., 2019; Mayolle et al., 2021; Visage et al., 2023). Despite this lack of dynamic description of damage growth, analogue modelling is still under-used, especially with new high-resolution devices. Nevertheless, fault damage zone growth with fault zone evolution remains poorly described and understood, even though the kinematics of each type of damage (approaching and intersection damage, wall, link, and tip damage) and the chronology of the damage structures and their distribution is important for the prediction of discontinuities affecting the rocks in the subsurface.

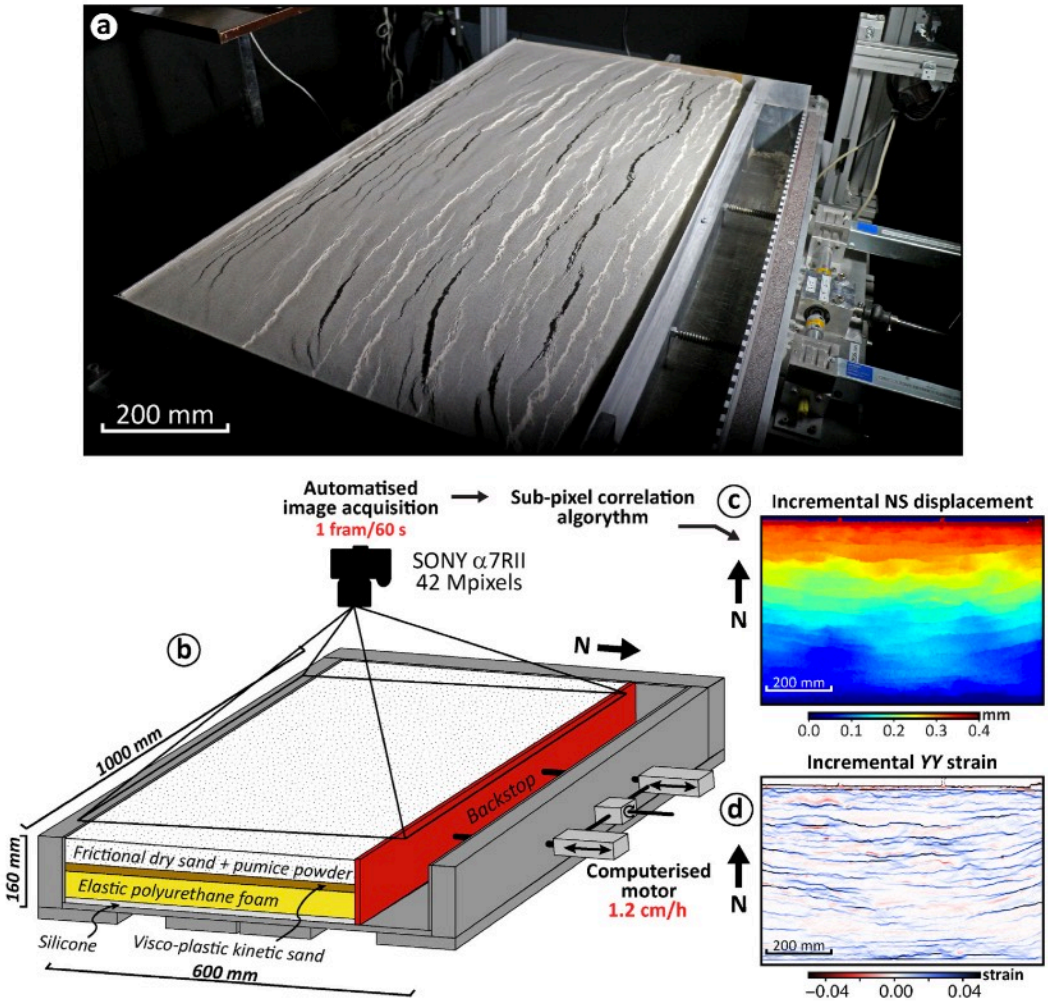

Fig. 1. a) Picture of the experimental device for analogue modelling of normal faults. b) 3D diagram of the experimental set-up showing model rheology in cross section and top surface imaged in this study. Examples of: c) incremental NS displacement field and d) incremental strain field *YY* (NS) derived from the displacement field in c).

In this study, we developed a sandbox analogue modelling setup equipped with high-resolution monitoring to focus on the map view evolution of fault damage through time along an entire fault system. With this aim, we first investigate the growth of a normal fault population by analysing images, strain field, and cumulative displacement gradient. Secondly, we describe the evolution of each type of fault damage zone at the macro and micro scale and mechanisms associated. This allows us to discuss how fault damage zones grow with respect to background damage, processes involved, and highlight new concepts of fault system damage patterns.

2. Experimental modelling

2.1. 3.1 model device and set-up

Normal fault analogue modelling allows the analysis and quantification of fault damage evolution and its lateral interaction during fault population growth. The experimental device is a 1 m long and 0.6 m wide box made of aluminum and equipped on one side with a mobile backstop controlled by a computerised motor allowing a constant speed of 1.2 cm/h (Fig. 1). For each picture and figures of the model surface in this study, the mobile backstop is on the upper part and moves to the North of the picture/figure.

2.1.1. Material composition and scaling

The model is made of two layers of granular material lying on a pre-compressed basal polyurethane foam (Fig. 1a and b). The upper layer of granular material is composed of 97.5% dry sand (HN38) with an average grain size of 150 μm, mixed with 2.5% of pumice powder with an average grain size of 43 μm. It has a bulk density of 1.4 g cm^3. The dynamic internal friction angle and associated cohesion were measured using a lab-made linear shear box device to $38^{\circ} \pm 1^{\circ}$ and 185 Pa ±20 Pa, respectively. The scaling between model and nature can be define by a dimensionless relation linking body (gravity) to surfaces (stress) forces (e.g. Hubbert, 1937; Davy and Cobbold, 1991), leading to the equation, $\sigma^* = \varrho^*.g^*.L^*$, where σ^*, ϱ^*, g^* and L^* are the model-to-nature ratio for cohesion, density, gravity and length, respectively. In experiments, g^* equals 1 and ϱ^* is about 0.6. L^*, imposed by experimental set-up and natural case studied dimensions, is about 10^{-5} (1 cm equivalent to ~1 km in nature), a standard value for sandbox analogue experiments (e.g. Schellart, 2002; Arzúa and Alejano, 2013; Reber et al., 2020). Using the previous equation, a cohesion of 185 Pa in the model corresponds to 30 MPa in nature, which is consistent for sedimentary rocks in general.

This analogue material layer has been tested with two different thicknesses, 50 mm and 80 mm. The lower layer is a mixture of 98% quartz sand of 150 μm mean grain size, and 2% PDMS silicone (poly-dimethylsiloxane). This material has a visco-plastic mechanical behavior and can be used to simulate a thick layer of shales, salt or the viscous middle crust (Mayolle et al., 2021; Zwaan et al., 2022). These two upper layers lie on a pre-compressed basal elastic polyurethane foam. A thin layer of silicone is also added at the base of the foam to prevent bulging during the pre-compression.

Distributed extensional strain is imposed by moving the lateral backstop at a speed of 12 mm/h. The maximum cumulated extension is 120 mm (20%) for all the performed models. The slight curvature of the fault traces observed at the surface of the model indicates that boundary effects exist but are very minor (Fig. 1a). Moreover, the lateral limits of the pictures are located 7 cm from the boundary of the model to avoid taking measurements from the areas where boundary effects are strongest (Fig. 1b).

2.1.2. Monitoring and strain field analysis

The experiment surface is monitored in map-view using a SONY α7RII camera taking one 42 Mpix 1 picture/60s at a resolution of 1 pixel = 109 μm (Fig. 1b). Pictures acquired during the experiments are processed using a sub-pixel spectral correlation algorithm based on Van Puymbroeck et al. (2000). This algorithm calculates, on a square window of 16, 32, or 64 pixels, the local offsets between two consecutive pictures, allowing quantification of the EW (u) and NS (v) incremental horizontal displacement fields. The image correlation methodology requires homogeneous and multidirectional lightning of the surface model to limit shadow areas (Fig. 2). Hence, four LED panels light up the surface model from each side of the device. For better visualisation of the faults at the surface of the model through time, pictures with low-angle light were taken every 15 min (Fig. 2).

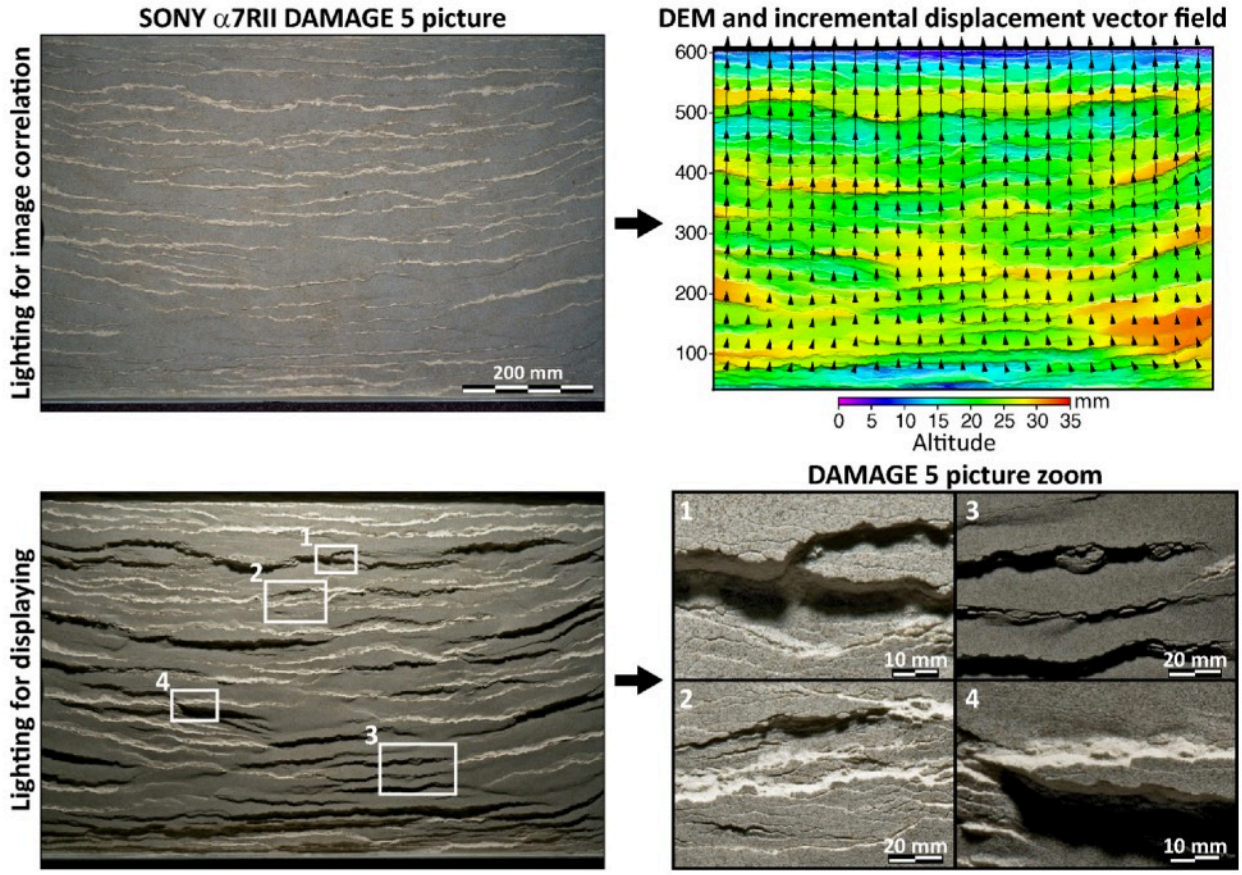

Fig. 2. Pictures of the DAMAGE 5 final stage, acquired by the SONY α 7RII with homogeneous light (upper) for image correlations and low-angle light (lower) for visualisation.

The quality of the correlation is also improved by sprinkling a mixture of microbeads, anthracite powder, and Camargue sand (160 μm) before starting the experiment. This mixture creates a fine and rich texture, each grain being imaged by only a few pixels. This texture allows a micrometric independent measurement of the horizontal surface deformation with a spatial resolution of 1–2 mm and a precision of few microns. The horizontal surface displacement field components are used to calculate two incremental strain fields; *XX* (EW), *YY* (NS). The deformations measured between each image are much less than 5%, and then a simplification of the Green-Lagrange formulation is used to calculate the strain fields. The strain fields *XX* and *YY* are derived respectively from the EW and NS displacement field. Note that the signal-to-noise ratio is always over 0.8, revealing the very high-quality of image correlation from which the displacement and strain fields are derived. The incremental displacement field allows calculating the cumulative displacement field. A point cloud is projected at the initial stage on the incremental EW and NS displacement field. Each point moves to new coordinates according to incremental displacement values and the point cloud provides a cumulative displacement field (U) of the model. Finally, the cumulative displacement gradient field (dU/dx, i.e. *grdgradient* function in GMT software (Wessel et al., 2013), the ampli- tude of the gradient) appears as the most relevant parameter to analyse fault damage zone deformation since it accounts for the absolute displacement (any direction). The vertical displacement component is measured at the final stage by digital photogrammetry processing softwares (MicMac and Meta-shape Pro).

2.1.3. Analogue material deformation

Five analogue models were performed, four experiments with the upper layer of the analogue material composed of 97.5% HN38 sand and 2.5% pumice powder, and one experiment using a material composed of 99% glass microbeads and 1% pumice powder. The thickness of the upper layer is 50 mm for two experiments (one of which is 99% microbeads) and 80 mm for three other experiments. Experimental results are presented using the fifth experiment DAMAGE 5 (97.5% HN38 and 2.5% pumice powder, 80 mm thickness), the measurements and structures of which are the most clearly imaged, and representative of the main results of our study. This material produces fractures which are observable at the model surface, as < 20 mm long and <1 mm open troughs (see supplementary material, Fig. S1), that generally correspond at depth in the model to very small disaggregation shears (<1 mm, see Supplementary Material Fig. S2). These fractures are qualified in this study as small segments or secondary faults (in the sense of Maerten et al., 2002; Kim et al., 2003, 2004), often having a shear component whose shear/opening ratio increases with their development and similar to those observed on rocks in shear box tests (Wibberley et al., 2000). Major faults developed further by a cumulative displacement of several millimeters (>100 m in nature) and a length of several tens of centimeters (>10 km in nature). Distributed deformation ("Hanging-wall folding") is also observed on the hanging wall of major faults and characterised by a tilting and a folding of the model surface over a range of a few millimeters to 1 cm from the surface fault trace. Finally, also note that the strain field generally reveals a distributed amount of deformation (see Supplementary Material Fig. S1b, generally around 10% of cumulative displacement) generally located around master and small faults. High-resolution images of distributed deformation reveal the absence of minor failure of the material (see supplementary material, Fig. S3), suggesting that deformation occurs as micro-scale deformation by grain

disaggregation (also see Mayolle et al., 2021). This deformation is considered to be dilatant, adjacent to major or secondary faults. Regarding the scaling of the material to nature, this very small-scale dilatancy within the host rock material is considered to be analogue to mode I fracture patterns or very small normal faults in nature. In places of hanging-wall folding, a contractional deformation can be observed (see section 3). This deformation might be only apparent by the effect of the hanging-wall tilting and producing a slight compaction of the material at the grain scale. In such cases, it can be considered as an analogue of very small thrust faults associated with fault propagation folding (Schlische, 1995; Peacock et al., 2000; With-jack et al., 2002; Jackson et al., 2006).

3. Results

3.1. Normal fault system evolution

From the onset of extension, heterogeneous deformation is detected across the entire model as relatively distributed (proto-)faulting, as shown by the incremental NS displacement field. After 2% of extension, the material starts localising the *YY* deformation along EW fault zones in response to the NS basal foam decompression imposed by the backstop retreat. During the first half of the experiment, the *YY* deformation tends to stabilise on 10 major faults located in the northern half of the model DAMAGE 5 (see supplementary material, Fig. S4a). The *YY* strain field also shows an intensity decrease from the faults to the host material between the faults and a slight deformation distributed in the tilted blocks. The *YY* strain field reveals extensional strain (blue) on and between the fault planes and more rarely contractional strain (red) on HW folds. In the second half of the experiment, the extension is distributed over the whole model. In between the major faults, the *YY* strain field has a lower intensity than the *XX* field by about one order of magnitude, highlighting the lateral strain occurring in the wall rock around fault surface irregularities and in overstep regions between fault segments. The cumulative displacement gradient shows a strain intensity increase on nearly all the master faults of the model. In detail, many small faults initiating in the first stages in between the master faults become inactive as the master faults continue to grow (this is more visible on the *YY* strain field). Once major faults are formed, they dominate the accommodation of the extensional strain, suppressing the activity on the smaller faults in the process.

3.2. Corridors of distributed deformation and small segments

The incremental *YY* strain field reveals how the first stages of extension are marked by the formation of a large number of segments and distributed deformation around them. The deformation is characterised between 0 and 3% of extension, by a heterogeneous distribution of the incremental strain over the material and a progressive strain localisation into zones of highly-variable width composed of a significant number of small segments. In this study, we defined these active zones with a width/length ratio between 0.05 and 0.2 as “corridors”. These corridors are of different scales, i.e. between 1 and 10 cm wide (see Fig. 3 at 1.2% extension, and sections 3.2.2. and 3.2.3.), and their thickness tends to decrease with increasing extension as deformation becomes progressively localised into major faults (Fig. 4a and b).

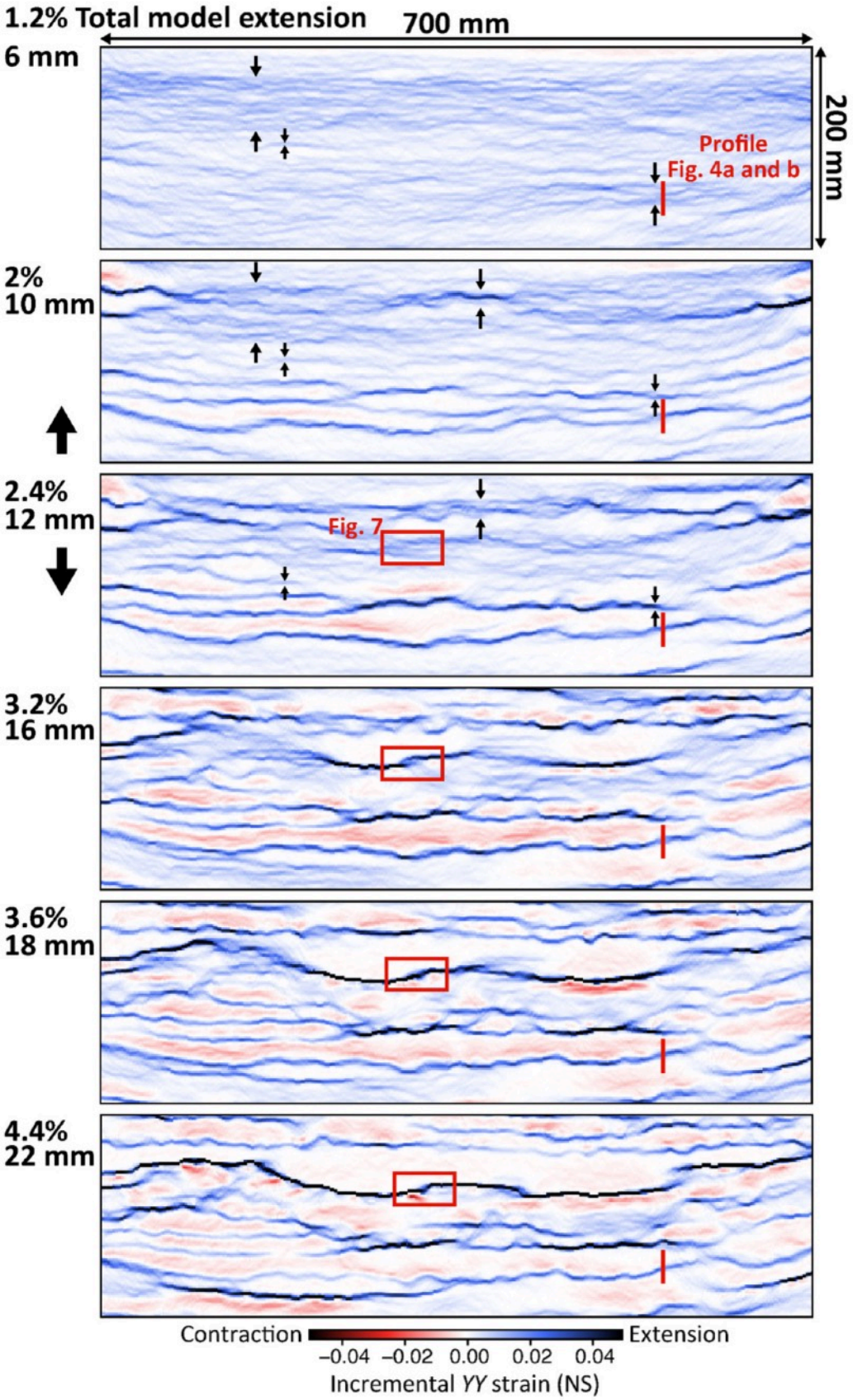

Fig. 3. Incremental *YY* (NS) strain evolution during early deformation of the DAMAGE 5 experiment. Each strain field shows the deformation between two images of the model, the extension between these images is 2 mm. Black arrows locate some corridors with different thicknesses.

Fig. 4 shows in a and b the evolution through time of the incremental *YY* strain into a corridor. The localisation of the incremental strain generates a reduction of the corridor width from 25 mm to 10 mm (Fig. 4). Within the corridors, linkage occurs with increasing strain into swarms of small fault segments having very little spacing (Fig. 3). Later stages in Fig. 3 illustrate how faults grow from these corridors through time, revealing that fault activity is located on few fault segments not homogeneously distributed through space and time. These segments are visible as 1–5 mm thick zones of concentrated incremental strain, particularly visible on Fig. 3 from about 2% extension onwards. Between 1% and 3% of extension, a localisation of the activity on specific fault segments occurs (Fig. 3) by fault segment interaction and linkage within the corridors and a subsequent development of master faults. Fault segment linkage occurs at different scales in the model (2–3 orders of magnitude of fault length) and accounts for the irregularities observed along the master faults in the later stages. Fault segment linkage also controls a rapid length growth of major faults with the increase of extension and displacement. The length and the lateral position of the major faults are determined by the length and width of corridors at the initial stage. Once the major fault localises the deformation (i.e. from 3.2% to 4.4% of extension), the displacement grows without significant increase in fault length by segment linkage or fault propagation. Corridors including small segments and the majority of the distributed deformation are abandoned, as shown by the white and red areas (no more extension) observed between the master faults (see supplementary material, Fig. S4). Some parts of this deformation are incorporated into the final damage zones of the master faults, other parts forming the background damage at the end of the experiment. Small faults and distributed deformation continue to occur in the later stages, but only in grabens, at fault tips and at relay zones, which are the main type of fault-related damage described below in section 3.3.

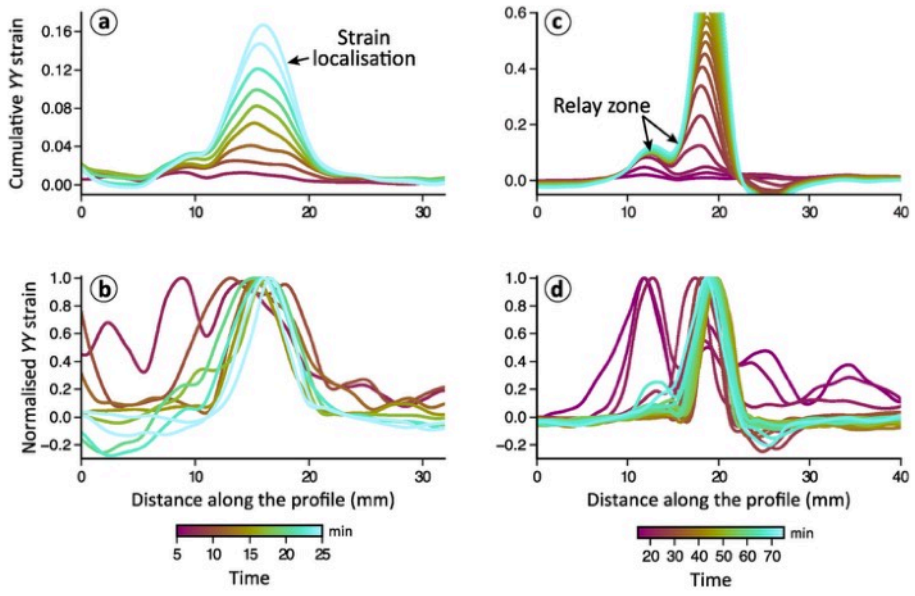

Fig. 4. Incremental *YY* strain profile evolution along a corridor with a localisation in single fault trace in a) and b) (Fig. 3), and along a corridor with a localisation in a relay zone in c) and d) (Fig. 7).

3.3. Damage zone evolution

3.3.1. Wall damage

Wall damage is difficult to observe due to its low lateral dimension. It is macroscopically composed of incorporated former segments, including secondary faults nearly parallel to the major faults, relay zones, and abandoned fault tips (Fig. 5a). Wall damage also includes hanging-wall folds resulting from the material flexure at the fault surface. These flexures generate a slight contraction in the fold axial zone, sometimes faulted, and form large damage zones of several millimeters to 1 cm from the main fault (Fig. 5).

In these wall damage structures, cumulative displacement gradients are higher than the background deformation over a distance of 1–5 mm from the faults. The cumulative displacement gradient has a maximum on the fault plane and decreases (between 20 and 50%) with increasing distance from the fault plane (1–5 mm of maximum distance) (Fig. 5a). The wall damage is better observed and measured on the footwall of the fault since damage in the hanging-wall is often masked by material collapse (analogous to landslides in nature).

3.3.2. Tip damage

Damage at the tip of isolated faults is difficult to observe because of the high fault density and interactions. Tip damage is characterised by segments a few millimeters long with fan or en echelon geometries located at (or around) the tip of the faults (see Supplementary Material Figs. S5a, b, c, d, e). These secondary faults are also accompanied by distributed micrometric deformation measured between them by image correlation (Fig. 5b). The *YY* strain shows a large and distributed micrometric deformation zone from the first stages of decreasing intensity (between 3 and 0.5%) from the fault plane to the tip (Fig. 6). The major fault is active along its entire length, which is composed of multiple small segments (steps 1 to 2, Fig. 6). Several segments develop preferentially (also see section 3.1) and connect over time from the fault center to its tip (from East to West, Fig. 6 steps 4 to 6).

Tip damage seems to have a limited propagation along the direction of the main fault (*i.e.* incipient deformation occurs in this place at the onset of the fault growth) unlike its thickness, which increases over time. Note that strain remains very low and close to the background deformation level (20% of the strain in tip damage is background deformation).

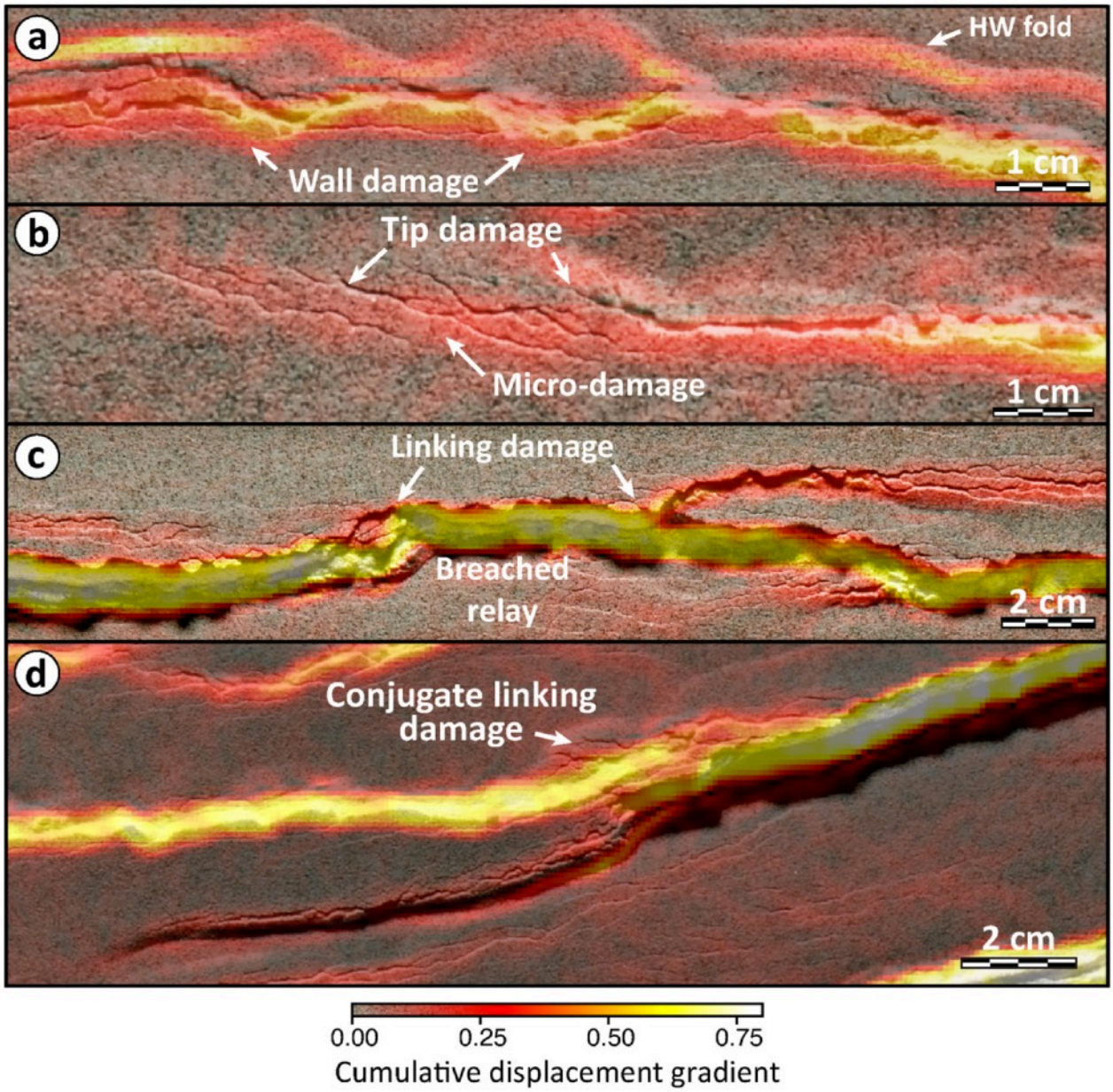

Fig. 5. a, b, c, d, e, and f, are examples of wall damage zones observed at model surface. Pictures are from the DAMAGE 5 experiment. g) The cumulative displacement gradient is superimposed on image f).

3.3.3. Linking damage

Fault growth by segment interaction and linkage is observed along numerous relay zones over two to three orders of magnitude of scale. Fault interaction and linkage is observed along two main categories; (1) relays as conventionally described in the literature, formed by the growth and interaction of two fault segments (Fig. 5c and see Supplementary Material Fig. S6 a, b, d, f, and g), and (2) between two former faults having a strong overlap acquired before their interaction and linkage. Interaction and linkage formed between two major sub-parallel segments generate numerous secondary faults oblique to the main segments. They contribute to the formation of a fully breached relay observed in these regions, which occurs with the increase of displacement. Linking damage zones are also composed of abandoned fault tips and secondary faults. These abandoned

structures contribute to widening the damage zone and to the cumulative displacement gradient decrease (between 25 and 50%) of several millimeters to 1 cm.

As mentioned in section 3.2, corridors composed of millimetric to centimetric length segments form in the material at the very first stages of extension (Figs. 3 and 7 A1, A2, B1, B2), which is also observed in places where macroscopic relay zones and fault linkage will occur. The coalescence of some fault segments creates millimetric to sub-millimetric size relay zones (Fig. 7 A2). This coalescence of fault segments at different scales also occurs along an axis that becomes the major fault trace in the later stages. The displacement increases on the segments by deformation localisation and the relay zone is finally linked or fully breached in the corridor zone established in the early stages (Fig. 7).

After breaching the relay zone, the deformation appears to be localised on a fault plane with a surface width close to those observed on either side of the relay on the incremental strain. During the increase of the deformation, the incremental strain shows a clear evolution from distributed to localised deformation on the fault plane after the linkage, while the cumulative displacement gradient shows an increase of the damage zone width (Fig. 4c and d). In the first stage of the model, the incremental deformation reveals that the above-mentioned corridor has a thickness around 30 mm (Fig. 7a), and subsequently localises into the relay zone, with a fault spacing of around 10 mm (Fig. 4c and d). At the final stage of the experiment, the full damage zone width and the structures formed from the initial stages of deformation and incorporated in the damage zone are manifested by the cumulative gradient field (Fig. 7 C6). These abandoned structures are not recorded in later stages of incremental strain field evolution once they become inactive.

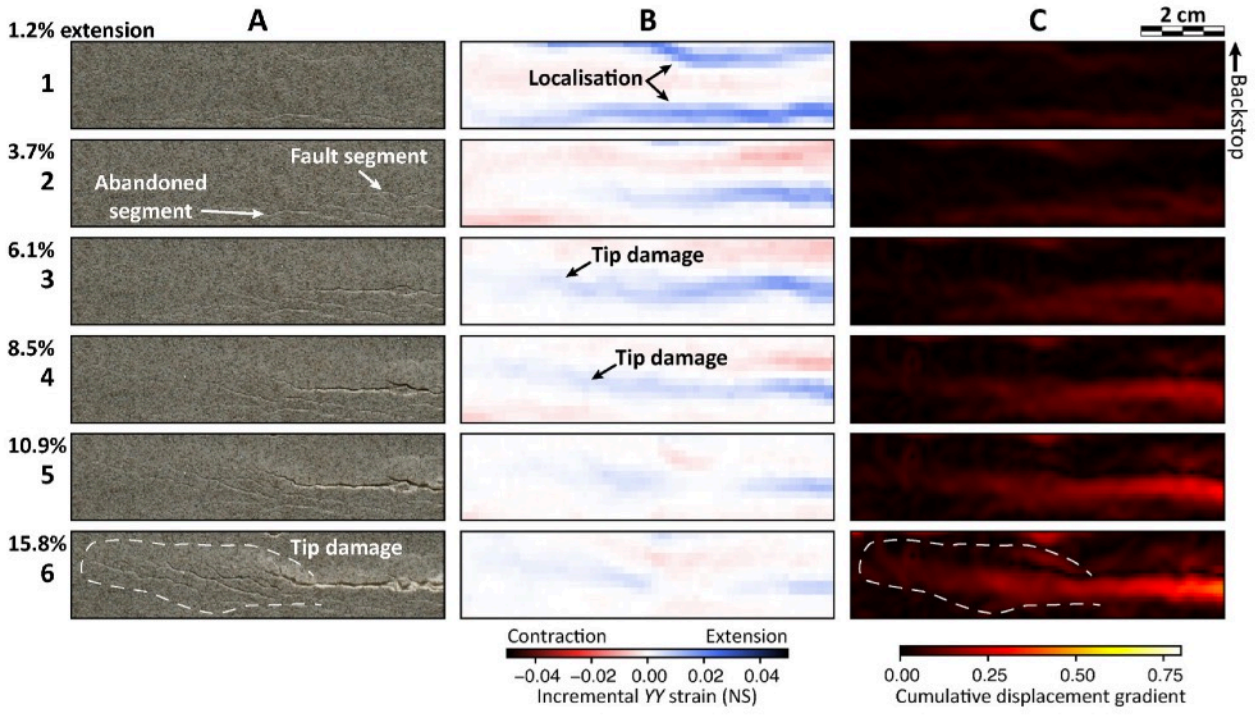

Fig. 6. DAMAGE 5 experiment: initiation and evolution of a tip damage zone. A) Pictures of DAMAGE 5 experiment surface. B) Incremental *YY* strain field. The increment used to calculate strain between two pictures is 0.4% (2 mm) of extension. C) Cumulative displacement gradient field.

3.3.4. Conjugate linking damage

Conjugate relay zones and displacement transfer between two conjugate normal faults are widely observed in the experimental dataset (see Supplementary Material Fig. S7). Convergent conjugate faults form small graben relays involving the two conjugate fault tips, with secondary faults and distributed deformation observed around and between the fault tips, over distances much larger than fault spacing in the relay zones (up to 4 times the spacing). These relay zones show conjugate segment interactions for fault spacing up to 10 mm. Divergent conjugate faults form a horst relay involving two conjugate fault tips spaced by less than 10 mm. The approaching damage develops by secondary faults and distributed deformation around faults in the horst part of the relay (Fig. 5d).

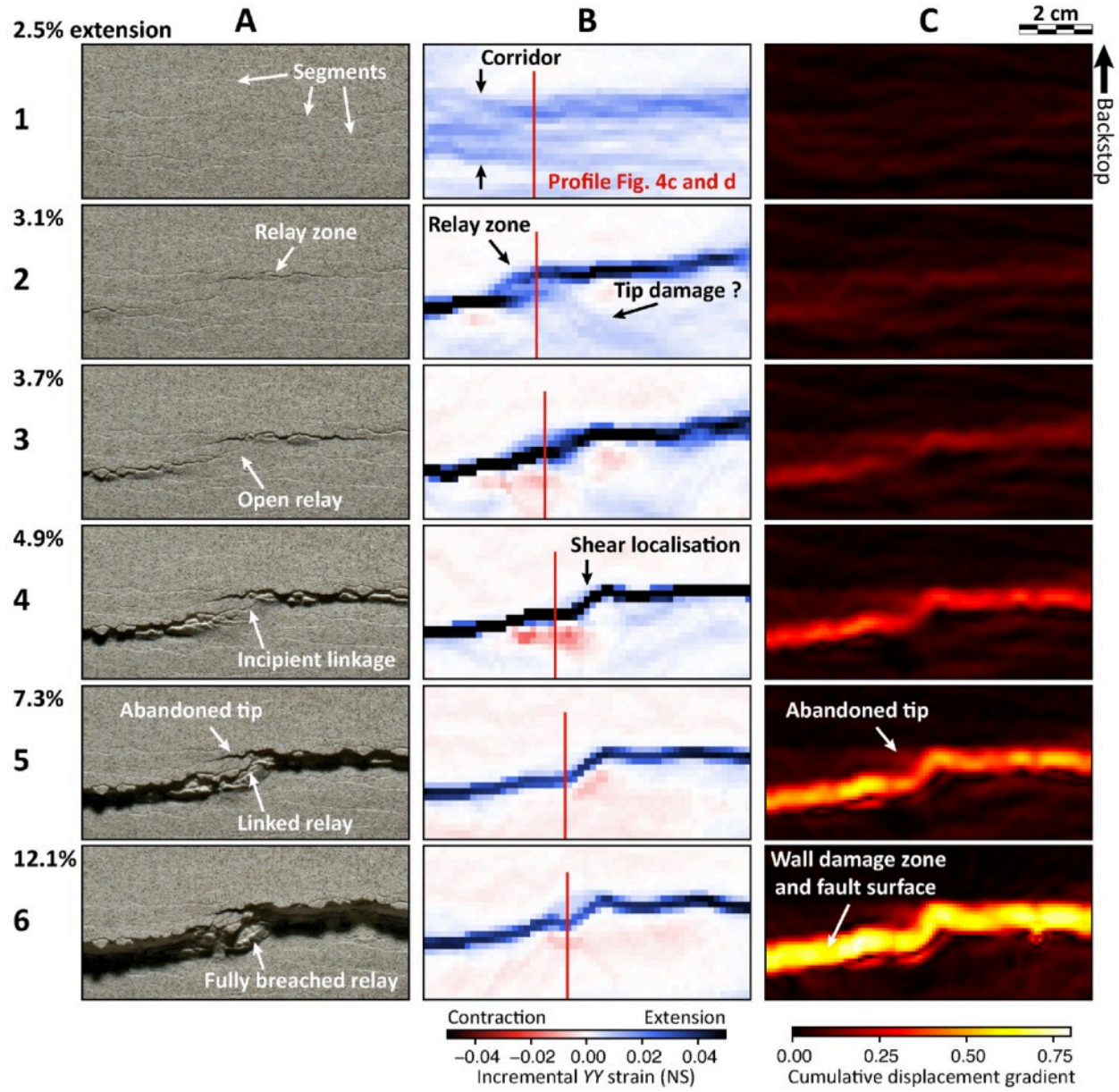

Fig. 7. DAMAGE 5 experiment: initiation and evolution of a linking damage zone. A) Pictures of DAMAGE 5 experiment surface. B) Incremental *YY* strain field. The increment used to calculate strain between two pictures is 0.4% (2 mm) of extension. C) Cumulative displacement gradient field.

These convergent and divergent conjugate fault relays are also characterised by a strong displacement gradient along the faults. While the displacement is about several millimeters on faults before the overlap zone of the relay, it can be close to 0 to a few millimeters laterally in the conjugate fault relay zone (see Supplementary Material Fig. S7c).

From the early stages of extension, the *YY* strain field shows localised deformation along an EW thin (5 mm–1 cm) corridor of deformation composed of many segments and distributed deformation (Fig. 8 A1 and B1). The segment corridor is developed on the length of the two future conjugate faults. The dip of the segments and of the master fault developed in this corridor is acquired in the very first stages of extension (A1). Then the two conjugate master faults initiate in this EW corridor with opposite dips (Fig. 8 A2 and B2). The western master fault dipping to the north remains active after linkage to the eastern master fault, but only propagates slightly further to the East, in the hanging-wall of the South-dipping fault (Fig. 8).

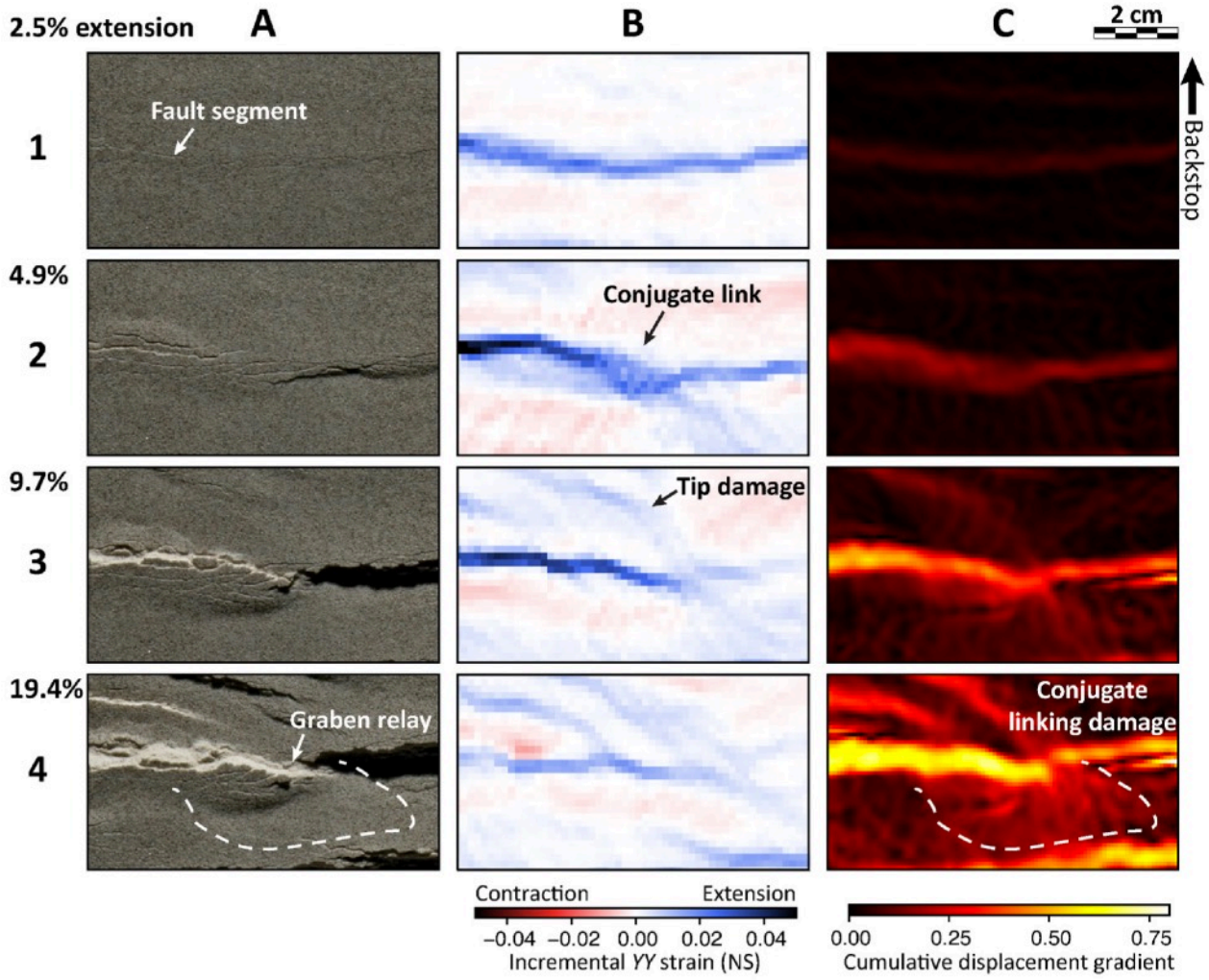

Fig. 8. DAMAGE 5 experiment: initiation and evolution of a conjugate linking damage zone. A) Pictures of the model surface evolution. B) Incremental *YY* strain field. The increment used to calculate strain between two pictures is 0.4% (2 mm) of extension. C) Cumulative displacement gradient field.

The incremental strain and cumulative displacement gradient also show that the distributed deformation in the tip damage of the western master fault generates a large and heterogeneous

damage in the foot-wall and hanging-wall of the western and eastern master faults. In the latter stages, the *YY* incremental strain field and the cumulative displacement gradient show distributed deformation and secondary faults located between and around the two conjugate fault tips, quite far from the relay (Fig. 8B and C, stages 3 and 4). The cumulative displacement gradient highlights the damage zone with values between 0.3 and 0.8 compared to the background values, which are less than 0.2.

Linking damage around these conjugate fault tips is generally characterised by strong asymmetry of the damage pattern out of the relay zone, both in the horst and graben relay configurations. Finally, also note that no clear master through-going fault develops in the relay zone during the last stages of fault segment linkage.

3.4. Graben damage

In all the experiments, large areas in the center of the grabens are affected by numerous secondary faults and large surfaces of distributed deformation around master faults but also around secondary faults (Fig. 9a, b, c). During the initiation stage, the master faults of the graben develop by segment interaction and linkage of some incipient faults initiating within corridors (Figs. 3 and 9). After the initiation of border faults and during their propagation by segment linkage, the incremental *YY* strain in corridors started localising, resulting in variable corridor width along-strike. As the extension increases, the deformation migrates from the outer graben border faults to the inner graben faults formed by segment interaction and linkage (Fig. 9c). New faults develop link, wall and tip process zones in the inner part of the graben with a frequency that decreases from the center towards the outer part of the graben (Fig. 10). Displacement variations along master faults induce block tilting and formation of secondary faults distant, oblique, and sometimes perpendicular to the major faults (Fig. 10 A3, B3). Also, note that in the center of the graben, the distributed deformation did not become localised, which is consistent with the increase of the cumulative displacement gradient reaching high values (up to 30%) and covering large areas (Figs. 9C and 10 B3 and C3).

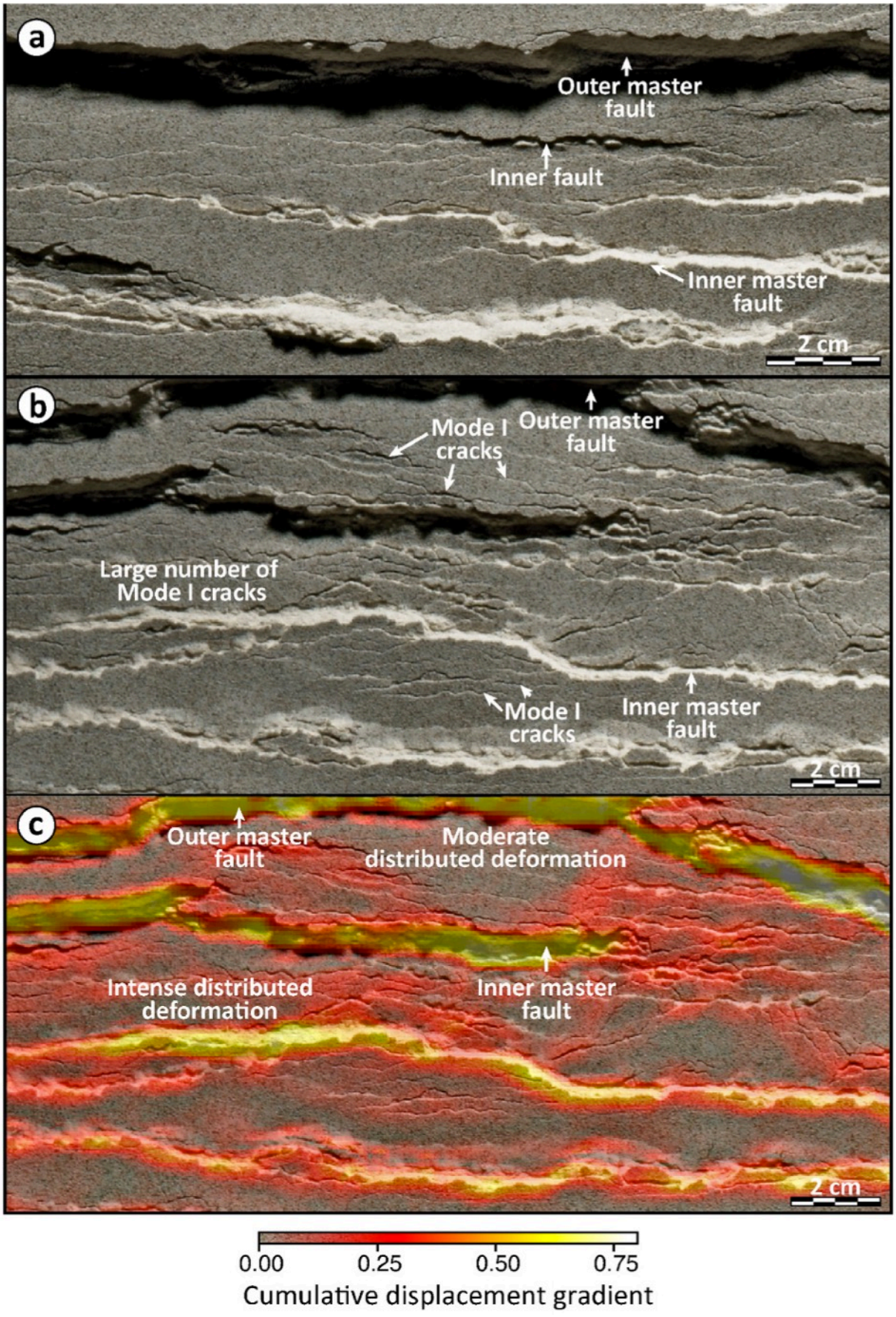

Fig. 9. Examples of graben damage observed on model surface. Pictures are from the DAMAGE 5 experiment and show several secondary faults in the inner part of the graben structure. c) The cumulative displacement gradient is superimposed on image b).

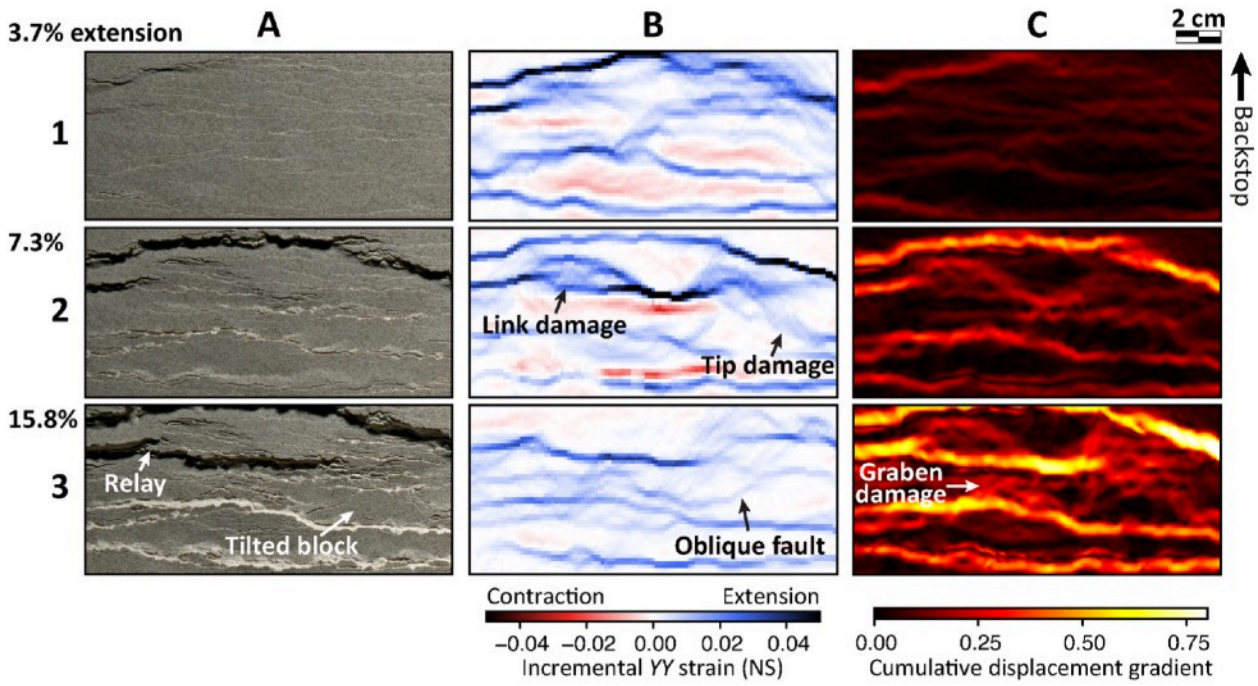

Fig. 10. DAMAGE 5 experiment: initiation and evolution of graben damage zone. A) Model surface evolution. B) Incremental *YY* strain field. The increment used to calculate strain between two pictures is 0.4% (2 mm) of extension. C) Cumulative displacement gradient field.

4. Discussion

The experimental analogue modelling used in this study reveals the kinematic evolution of wall, tip, and linking damage, and also allowed the description of poorly-described structures such as "graben damage" and "conjugate linking damage". Detailed drawings of characteristic examples of fault damage types and related distributed deformation are presented in Fig. 11 to summarise the results. We describe the development of these structures firstly by the development of corridors of distributed deformation, followed by the growth and coalescence of fault segments within them.

4.1. Analogue modelling limits

It is worth considering that the analogue material and boundary conditions used have several limitations. One of the most significant is the impossibility to develop trans-granular fractures. The mean grain size in the model is 150 μm, corresponding in nature to about 10 m. The material used is therefore inappropriate to reproduce mode I fractures. In the model, the small mode I fractures visible by their sub-millimeter opening are considered equivalent to secondary faults with a displacement lower than 50–70 m in nature. However, the distributed deformation revealed by strain field measurements can be considered equivalent to mode I fracture deformation in nature, measured along scanlines. This deformation observed at the granular scale (e.g. Fig. 5, also see supplementary material) decreases with increasing distance from the fault plane, just as fracture frequency decays moving away from the main fault in natural fault damage zones.

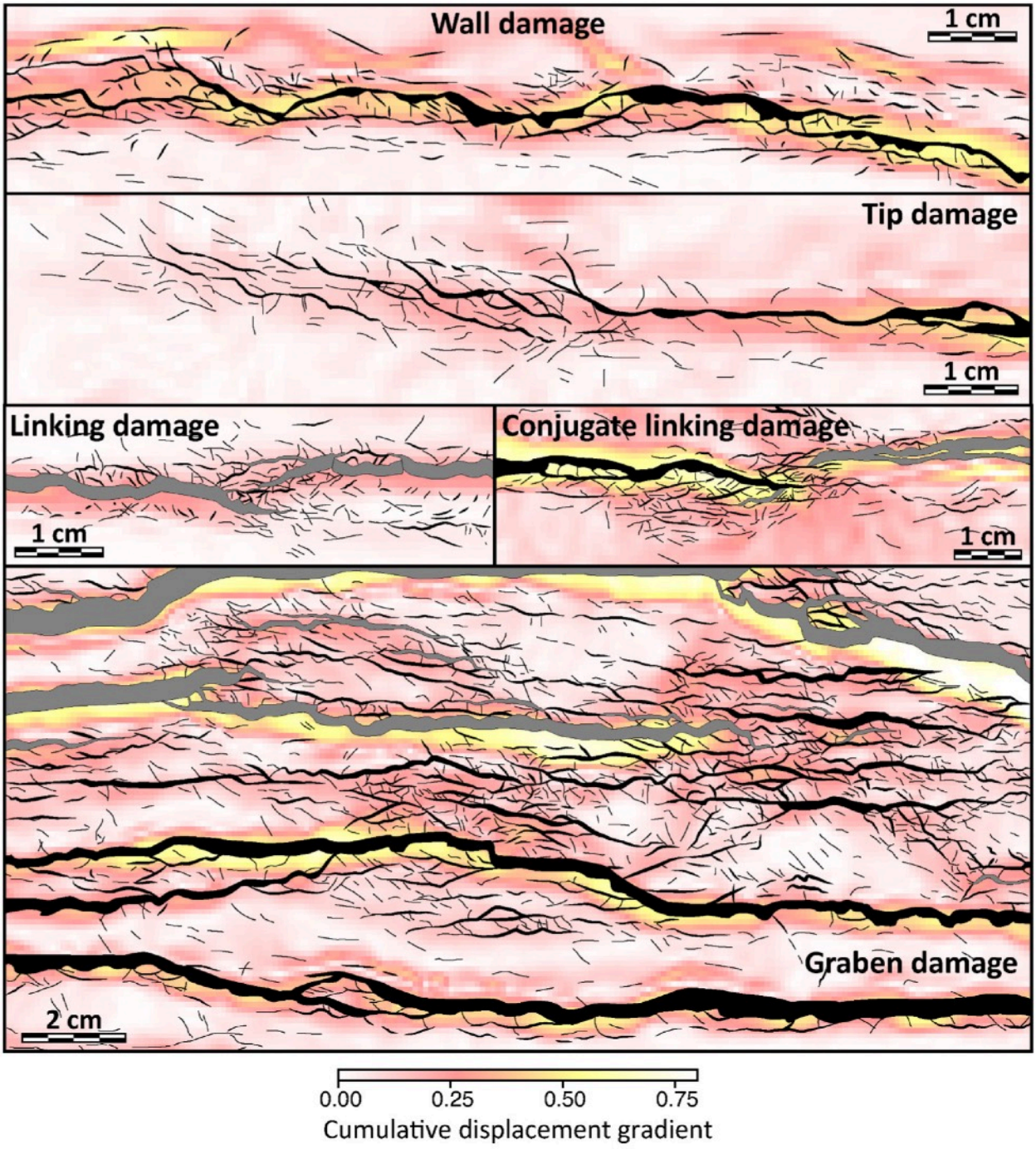

Fig. 11. Interpretative drawing of fault damage zone types superimposed on cumulative displacement gradient. The grey fault planes are dipping to the south and the black fault planes to the north. Thin black lines denote Mode I cracks at the surface of the model.

In the absence of trans-granular fractures, fault rocks and cataclasis cannot be reproduced. Fault cores are however present in the material as zones of dilatant to compactant shear disaggregation, with thickness lower than 2 mm (Mayolle et al., 2021). On the other hand, the granular scale reproduces correctly the geometry and scaling properties in populations of hundred-meters long natural faults (e.g. Bellahsen et al., 2003; Schlagenhauf et al., 2008; Mayolle et al., 2021). Both

geometric features such as dip angles, segmentation, and conjugate fault geometries, as well as scaling law characteristics such as *Displacement - Thickness* and *Displacement - Length* relationships, are properly reproduced (Schlagenhauf et al., 2008; Mayolle et al., 2021).

Other limitations of the model, considered of second order, concern boundary effects. The first boundary effect to discuss is the use of a pre-compressed foam at the base of the model. Although it avoids velocity discontinuity at depth, it has in turn the effect of distributing the extensional deformation quite homogeneously in the above sand layers, a condition which is well represented in nature (e.g. Afar depression, Basin and Range), and does not preclude the process of strain localisation from multiple segments to single master faults observed both in wide and narrow rifts.

The second boundary effect to consider is related to the presence of lateral walls limiting the EW propagation of faults and inducing rotations of the principal stress trajectories. This effect has been reduced by using a very low friction Teflon film along the lateral walls. This effect only implies 5–10 cm wide zone close to the walls where fault orientations change. These zones have been avoided to study fault damage evolution.

Another type of limitation having some implication on the horizontal strain field calculation is related to the tilting of the model surface along HW folds in the hanging-walls close to the fault or in blocks delimited by two synthetic main faults (Fig. 10). This rotation has been double checked by analysing the models in cross-section at the end of the experiment (Mayolle et al., 2021; supplementary material). Results suggest that this effect is the main process explaining the contractional strain observed at the surface of the model. This effect produces apparent horizontal contraction up to a maximum of 2.5% in some HW folds and up to 1% in the blocks between the faults. This bias is probably very important in HW folds adjacent to faults, as for example in the red area close to the main faults in Figs. 7 and 10. Note that it cannot be corrected since it would require the acquisition of extremely fine DEM of the model surface at a very large sampling rate at each image taken. Fortunately, most of the surface of the model is not significantly tilted, implying little bias (≤1%) on strain field calculation in general. Note that another negligible bias can be generated by a small drift during the cumulative strain field calculation, implying little bias (≤2%) on strain field calculation in general.

One last limitation of the analogue models is the absence of observations at depth during the experiments. However, we have significant amounts of data and complementary analysis of fault propagation and damage zone evolution from analogue models analysed in section view through a lateral glass wall, with variable layer thicknesses, and similar material conditions to the present study (Fig. 12, also see Mayolle et al., 2021, for more detailed information). We observe the same processes in cross-section view, revealing that localisation of deformation into corridors of distributed incremental strain also occurs at depth nearly simultaneously with that at the surface of the model (Fig. 12, also see Mayolle et al., 2021).

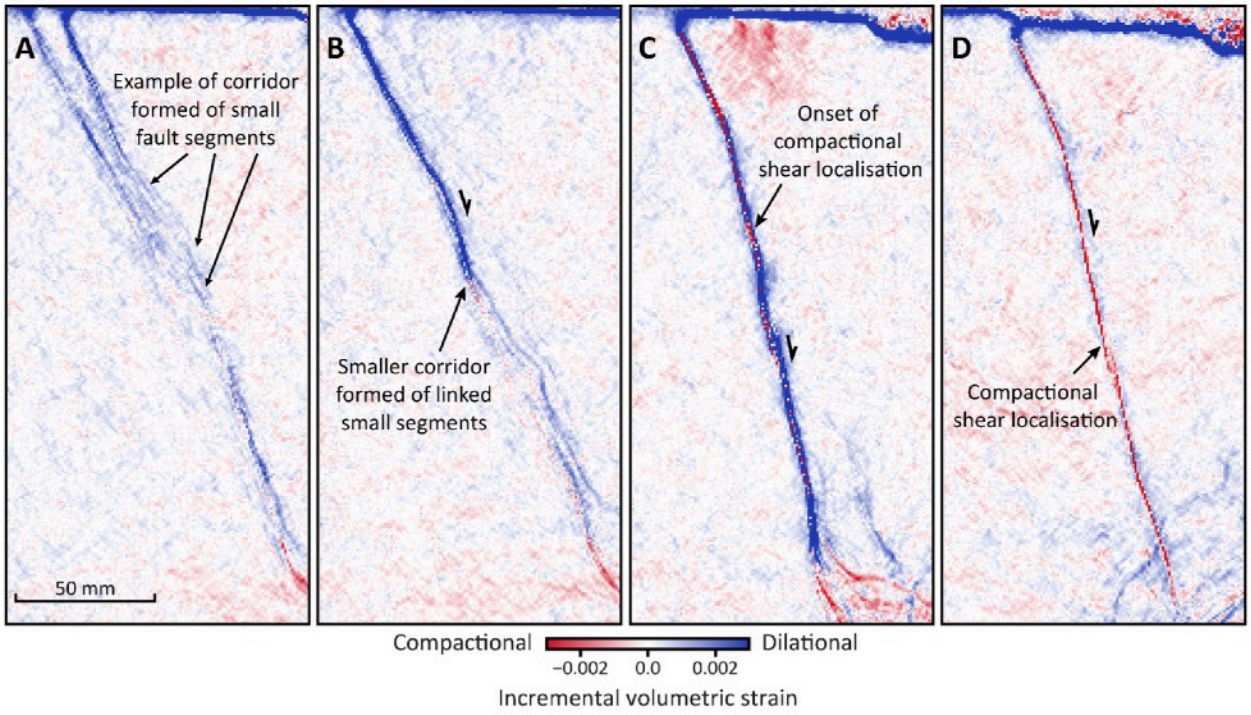

Fig. 12. Incremental volumetric strain evolution of a normal fault in cross-section view (modified from Mayolle et al., 2021). The fault corridor in cross-section is not related to fault propagation at depth (A). The incremental deformation localised with the increase of extension as in map view in this study (B and C).

4.2. Growth of tip, linking, conjugate linking and wall damages

Most of the damage types described in the literature, such as tip, wall and linking damages (e.g. Kim et al., 2004; Perrin et al., 2016; Choi et al., 2016; Peacock et al., 2017) are well reproduced in our models. The novelty in this paper is the description of their growth with increasing deformation, and especially the fact that they develop by heterogeneous strain localisation into corridors of distributed strain and small segments (see the next section 4.3 for further details), due to the presence of swarms of small segments, very early on in the experiments, favoring their linkage. Then, as proposed by previous authors (e.g. Walsh et al., 2002; Nicol et al., 2005; Jackson and Rotevatn, 2013; Rotevatn et al., 2019), the faults do not really propagate but developed within previously acquired deformation (corridors). Here we show that these corridors evolve through time by reducing their thickness as fault segment linkage occurs and strain localises into them, and that the different types of damage are inconsistent with the propagation model (e.g. Fig. 3, Fig. 6, Fig. 7, and Fig. 13). We also show that wall damage is composed both of distributed deformation, and of tip and link damages developed previously in the corridors (Fig. 13).

We also describe for the first time the evolution of *conjugate linking damage* in the out-of-plane dimension of the fault slip. Conjugate linking damages are hybrid zones of approaching damage with interactions between tip and linking damage structures of faults having opposite dip (Peacock et al., 2017). Linkage between conjugate faults has been identified as common feature in normal fault systems (Morley et al., 1990; Morley, 1995; Withjack et al., 2002; Childs et al., 2019). The damage associated with these structures is also identified in cross-section view (Nicol et al., 1995; Watterson et al., 1998; Ferrill et al., 2009; Peacock et al., 2017) without describing in detail the

damage pattern in the out-of-plane view of normal faults. With respect to spacing and the relative positions of the faults, the damage pattern is expected to be more or less pronounced and also organised following two specific configurations; horst or graben relays (Morley et al., 1990; Ferrill et al., 2009).

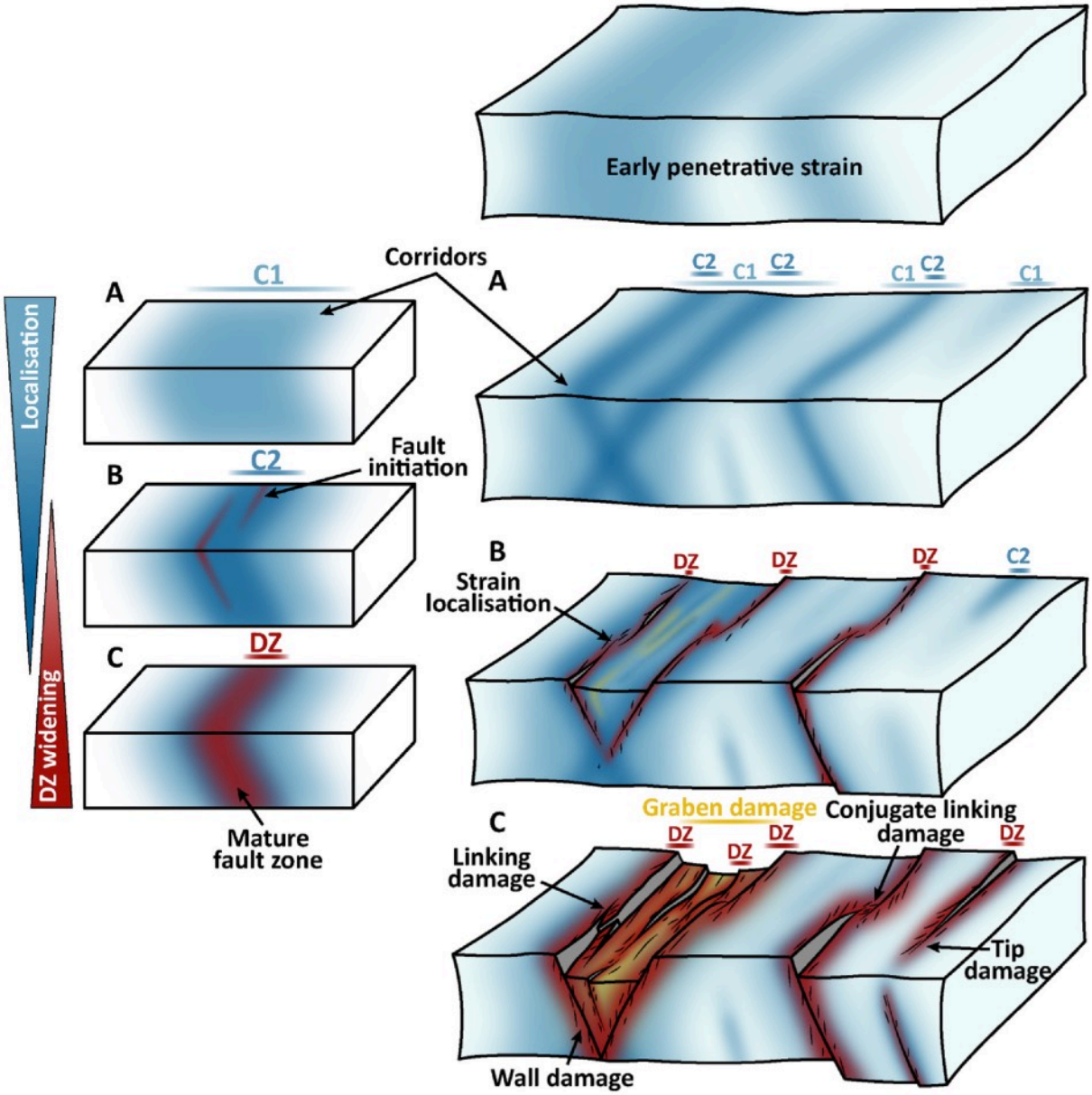

Fig. 13. Conceptual model of fault segment corridors and fault zone growth. A) the first stage of the deformation shows low penetrative strain, composed small of fault segments corridors and distributed deformation. B) the corridor deformation gradually localises by segment linkage process and major faults are initiated. C) the deformation is localised on fault planes, the fault damage zones thicken and the corridors are inactive and form a part of the background damage and fault damage.

The damage pattern is particularly pronounced into graben relays also surrounded by significant fault damage around the relay as observed in the strain field (Fig. 8). This is probably the consequence of the high displacement gradient due to impeded propagation and its heterogeneity observed along the master faults involved in the graben relay (Fig. 8c, step 4). High lateral

displacement gradient along fault must imply a significant amount of adjacent off fault deformation (Childs et al., 2019). This process seems to be more pronounced in graben relays rather than horst relays, probably because their difference in fault configuration implies differences in the ability of faults to propagate, overlap and link. This physical barrier to fault propagation probably generates conditions for strong heterogeneity of displacement gradient observed along faults (also see Childs et al., 2019).

4.3. Fault system damages: wide corridors and graben damages

We define "fault system damage" as any distributed deformation that can be considered as background damage occurring during fault system growth. Fault system damage is not directly related to the growth of a single master fault at the time this damage develops. Fault system damage is therefore different to any distributed brittle deformation formed by processes other than fault system growth, e.g. burial, uplift, thermal processes (e.g. Pollard and Aydin, 1988; Bourne, 2003). In our case, fault system damage corresponds to distributed deformation observed as wide corridors formed previously to master faults (Fig. 3, Fig. 4 and Fig. 13), and also graben damage described as strain distribution between conjugate master faults (Fig. 9, Fig. 10, Fig. 11, Fig. 13 and Fig. 14).

In the first type of fault system damage, i.e. wide corridors, the small segments formed in the initial stages correspond only to very small amounts of deformation (no more than 3% of the total cumulative displacement). This very small deformation compared to the cumulative displacement observed around faults (about 30%, in red for example in Fig. 5f) mostly contributes to what could be considered as background deformation measured between the master faults in the last stages. As shown by the different fault damage types described, the observed and measured damage zones of the master faults in the final stages corre- spond more to the structures formed by interaction and linkages of large fault segments, developed within the corridors. The size of the relay width, spacing and linkage increase with increasing strain in corridors, in accordance with datasets of natural fault zones (e.g. Soliva and Benedicto, 2004; Childs et al., 2009).

These corridors are only observed on the incremental strain field (e. g. Figs. 3 and 7), which probably explains why such structures were poorly identified and described from field data or analogue models to date. Their active thickness reduces with increasing cumulative strain (e.g. Fig. 3), which might be considered as inconsistent with respect to the scaling of damage zone thickness to fault displacement described in the literature (e.g. Savage and Brodsky, 2011; Mayolle et al., 2019). Considering that fault damage zones are estimated in the field with respect to background deformation, and that none of the field studies allows the analyses of the entire fracture pattern between faults, such a pattern of corridors of small segments and distributed deformation (fractures) is therefore extremely difficult to describe on a full fault system, and therefore not considered in the *damage zone thickness – displacement* scaling data. It is well known that faults grow by segment linkage from multiple small faults that evolve into a single master fault (Cowie et al., 1995; Gupta and Scholz, 1998; Ackermann et al., 2001; Soliva et al., 2008; Rotevatn et al., 2019).

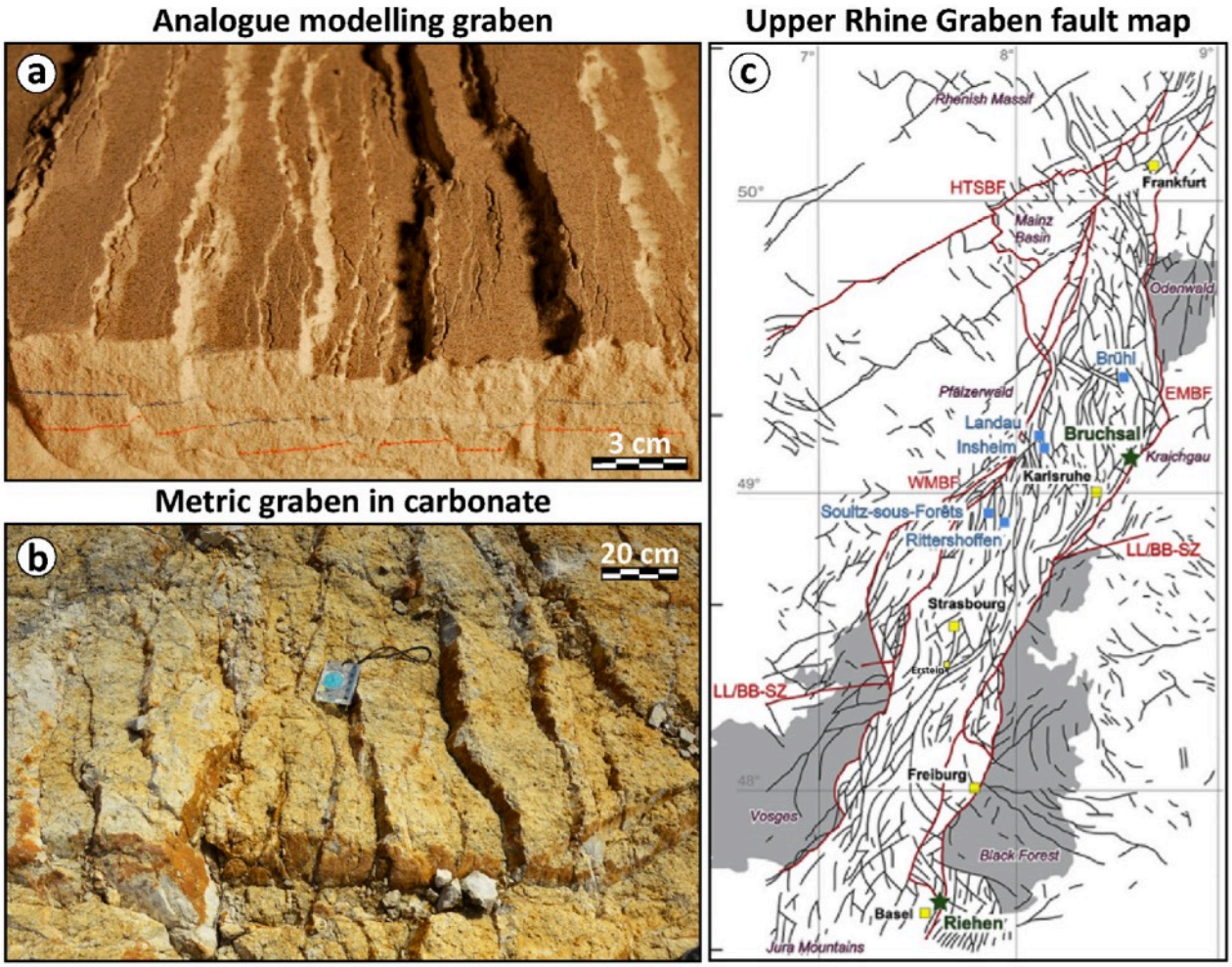

Fig. 14. Graben damage comparison between a) analogue modelling of this study in cross-section view, b) graben in carbonate rocks at metric scale and c) the upper Rhine graben fault map at kilometer scale (modified from Meixner et al., 2016). These examples show many small faults, in the center part of the graben, laterally limited by the main faults.

The location of a corridor of small fault segments able to link probably determines the position of larger faults formed by segment linkage. The newly formed faults interact with more distant segments within the initial corridors, but at a stage where the small segments and distributed deformation seem no longer active. Once the formerly segmented faults are large enough compared to other unlinked segments, they have better ability to release shear stresses within larger volumes in their vicinity, suppressing activity on adjacent segments of smaller sizes (anticlustering process, e.g. Segall and Pollard 1980; Ackermann and Schische, 1997; Gupta and Scholz 2000). This process, leading to the abandonment of the smaller segments (Fig. 6, e.g., Peacock and Sanderson, 1991), is probably enhanced by the efficiency of fault segments to be larger, and probably contributes to localisation of activity into zones within the corridors. Most of fault segments stop growing at different stages during the experiment although they reach a significant length, while other fault segments develop in adjacent zones (Fig. 3). Lateral segment linkage and length increase also seems to be a function of the presence of crossing conjugate faults acting as barriers to propagation at their lateral tips (graben relay), but also of processes occurring in the vertical dimension such as vertical linkage of fault segments (Fig. 13, e.g. Mayolle et al., 2021). This vertical segmentation and strain localisation into a brittle layer is probably responsible for the

limited thickness of mature faults (e.g. Mitchell and Faulkner, 2009; Savage and Brodsky, 2011; Solum and Huisman, 2017; Balsamo et al., 2019), as proposed in Mayolle et al. (2019), 2021. However, it is also possible that the presence of corridors prior to incremental strain localisation has an impact on the limited widening of fault damage zones, in that stronger material outside the corridors should be more difficult to damage, especially when the fault core weakens and stress drops occur around faults.

The reasons for the initial location and thickness of the corridors are unclear. Although the presence of the foam and the silicon at the base of the model aims to optimise the distribution of strain imposed on the sand, it may control the properties of corridors and evolution of faults into them. Relaxation of the foam is probably not perfectly homogeneously distributed through time, similar to likely behavior of the basement or the lower crust in nature. This may explain why some master faults are impeded from growing at some point and other zones and faults better develop and produce border faults in rifts.

Through time, the incremental strain localises while the cumulative displacement gradient increases in amplitude and thickness. More precisely, the distributed incremental deformation organised in corridors becomes more localised (Fig. 4) as fault segments grow by linkage and relay zones between the master segments can be larger (Fig. 3, also see Fig. 9 in Mayolle et al., 2019). This results in the narrowing of deformation of corridors while the cumulative deformation around the master faults is widening by segment linkage (Fig. 13). The narrowing of the incremental strain corridor, in nature, may be consistent with both the existence of background fractures in the field having the same trend as faults, and also the presence of fracture corridors in regions of small strain (few faults, e.g. Sanderson and Peacock, 2019). The difference of deformation evolution observed between incremental and cumulative deformation fields in our models is consistent with the difference of strain distribution evolution observed in experimental modelling and field observations. Indeed, experimental modelling generally reveals incremental strain localisation (e.g. Tapponier and Brace, 1976; Bésuelle and Lanatà, 2016; Papamichos et al., 2017), whereas geologists generally measure the widening of cumulative strain (Savage and Brodsky, 2011; Mayolle et al., 2019). Eventually, heterogeneous background damage as described has been observed both in experiments and nature (e.g. Jorand et al., 2012; Trice et al., 2018), and related to inhomogeneous stress conditions and/or material properties.

The second type of fault system damage described in this paper is the “graben damage”, corresponding to zones with high densities of secondary faults in a large volume of material between conjugate faults. Graben damage described in the model shows analogous similarities to the damage pattern observed at large or small scale (see for example the fault system of the Upper Rhine graben, and outcrop observations in carbonate rocks Languedoc, Fig. 14) also showing high densities of secondary faults in the internal part of the graben compared to its flanks (Illies and Greiner, 1979; Meixner et al., 2014; Trippanera et al., 2015). Contrarily to the other fault damage types, graben damage is not related to single faults or relay zones, instead generating distributed, small segments which can evolve into quite large faults along wide surfaces between conjugate faults, and can therefore be considered as a “fault system damage”.

More generally, these damage types raise the problem of damage zone classification and the problem related to how DZ thickness should be considered from field data (Peacock et al., 2017). The commonly described damage zones are often the result of segment linkage processes, so that wall damage contains a significant part of tip and linking damages and therefore are hybrid damaged type areas. The increase of the number of damage types such as provided in this paper, accounts for the strong heterogeneity of damage patterns, processes of fault growth and reveal how much fault thickness definition is dependent on the scale of analysis and quality of outcrop exposure, both in the immediate vicinity of a fault, and in between faults.

5. Conclusions

In this paper, we present new results about the evolution of fault damage types based on high-resolution analogue modelling. The main results are:

1. From the incremental strain field analysis, corridors of low penetrative strain were identified, in the form of small fault segments and distributed deformation. These corridors form in the first stages of deformation and reduce in active size as strain increases. They host the processes of segment interaction and linkage leading to strain localisation as master faults in advanced stages of deformation. These corridors become inactive and form parts of both background and fault damages in the later stages of fault growth.

2. Linking, tip, and wall damage evolutions are described for the first time from analogue modelling, from initiation to maturation and with respect to fault system growth. These structures do not form by dominant propagation processes but by linkage of previously formed small segments. Fault damage zones and their variable thicknesses are mainly the results of fault segment linkage processes occurring within the corridors. Linkage at fault relays allows the growth of master faults and the suppression of activity on small secondary faults formed earlier within and around the relay zones. This inactive damage becomes incorporated into the master fault zone as wall damage.

3. We observe conjugate linking damage newly described in the out-of-plane view. This damage seems particularly asymmetric and large around faults. Such fault configuration inhibits the lateral propagation of the two conjugate main faults during their linkage, which probably accounts for this wide off-fault damage.

4. Another type of damage has been described, the graben damage, which highlights a new concept of fault system damage. Fault system damage is an increase of damage structural density not specifically related to one fault, but resulting from fault system strain localisation leading to interaction of several master faults.

Overall, this new study of analogue experimental models reveals for the first time how fault damage zones evolve through time and space and how they are controlled by fault segmentation into corridors of distributed deformation. It also reveals how the nature of fault nucleation and localisation in a brittle/frictional layer strongly impacts the later stages of fault growth and resulting final fault zone geometry. Hence damage zones should not necessarily be considered as related to one fault, but as part of an evolving system of faults which interact and grow together as the geological strain increases. This description of the growth of brittle deformation around master fault tips, relay zones, linking geometries and into grabens, improves understanding of how active zones of deformation evolve through space and time in fault systems, and in particular provides a more complete view of damage patterns. This therefore provides new insight into the spatio-temporal evolution of zones of permeability enhancement in the Earth's crust and particularly the localisation of conduits within naturally fractured reservoirs. This is important for prediction of such conduits for targeting zones of enhanced productivity in reservoirs, prediction and mitigation of cap rock integrity issues in storage sites, for geothermal resources, and the assessment of micro and macro seismicity and hydro-mechanical properties of fault zones in general.

Credit authorship contribution statement:

Sylvain Mayolle: Methodology, Formal analysis, Investigation, Visualization, Writing – original draft. **Roger Soliva:** Conceptualization, Funding acquisition, Supervision, Investigation, Writing – original draft. **Stéphane Dominguez:** Methodology, Formal analysis, Investigation, Resources, Writing – review & editing. **Christopher Wibberley:** Conceptualization, Supervision, Funding acquisition, Writing – review & editing.

Declaration of competing interest:

The authors declare that they have no known competing financial interests or personal relationships that could have appeared to influence the work reported in this paper.

Data availability: Data will be made available on request.

Acknowledgments:

TotalEnergies SA, University of Montpellier and G´eosciences Montpellier provided financial support for this research developed during the DAMAGE research program hosted at the University of Montpellier. The experiments were conducted at the Laboratoire de Modélisation Analogique in Géosciences Montpellier (https://modelanalogique.gm. univ-montp2.fr/). We thank the editor and anonymous reviewers for their helpful reviews. We thank C. Romano for technical assistance. We also thank Wessel et al. (2013) for using GMT software.

Appendix A. Supplementary data

Supplementary data to this article can be found online at https://doi. org/10.1016/j.jsg.2023.104975.

References

Ackermann, R.V., Schlische, R.W., 1997. Anticlustering of small normal faults around larger faults. Geology 25, 1127–1130.

Ackermann, R.V., Schlische, R.W., Withjack, M.O., 2001. The geometric and statistical evolution of normal fault systems: an experimental study of the effects of mechanical layer thickness on scaling laws. J. Struct. Geol. 23, 1803–1819. https://doi.org/ 10.1016/S0191-8141(01)00028-1.

Alongi, T., Brodsky, E.E., Kluesner, J., Brothers, D., 2022. Using active source seismology to image the Palos Verdes Fault damage zone as a function of distance, depth, and geology. Earth Planet Sci. Lett. 600, 117871 https://doi.org/10.1016/j. epsl.2022.117871.

Ampuero, J.P., Mao, X., 2017. Upper limit on damage zone thickness controlled by seismogenic depth. In: Thomas, M.Y., Mitchell, T.M., Bhat, H.S. (Eds.), Geophysical Monograph Series. John Wiley & Sons, Inc., Hoboken, NJ, USA, pp. 243–253. https://doi.org/10.1002/9781119156895.ch13.

Arzúa, J., Alejano, L.R., 2013. Dilation in granite during servo-controlled triaxial strength tests. Int. J. Rock Mech. Min. Sci. 61, 43–56. https://doi.org/10.1016/j. ijrmms.2013.02.007.

Balsamo, F., Clemenzi, L., Storti, F., Solum, J., Taberner, C., 2019. Tectonic control on vein attributes and deformation intensity in fault damage zones affecting Natih platform carbonates, Jabal Qusaybah, North Oman. J. Struct. Geol. 122, 38–57. https://doi.org/10.1016/j.jsg.2019.02.009.

Beach, A., Welbon, A.I., Brockbank, P.J., McCallum, J.E., 1999. Reservoir damage around faults; outcrop examples from the Suez Rift. Petrol. Geosci. 5, 109–116. https://doi.org/10.1144/petgeo.5.2.109.

Bellahsen, N., Daniel, J.M., 2005. Fault reactivation control on normal fault growth: an experimental study. J. Struct. Geol. 27, 769–780. https://doi.org/10.1016/j. jsg.2004.12.003.

Bellahsen, N., Daniel, J.-M., Bollinger, L., Burov, E., 2003. Influence of viscous layers on the growth of normal faults: insights from experimental and numerical models.
J. Struct. Geol. 25, 1471–1485. https://doi.org/10.1016/S0191-8141(02)00185-2.

Berg, S.S., Skar, T., 2005. Controls on damage zone asymmetry of a normal fault zone: outcrop analyses of a segment of the Moab fault, SE Utah. J. Struct. Geol. 27, 1803–1822. https://doi.org/10.1016/j.jsg. 2005.04.012.

Bésuelle, P., Lanatà, P., 2016. A new true triaxial cell for field measurements on rock specimens and its use in the characterization of strain localization on a vosges sandstone during a plane strain compression test. Geotech. Test J. 39, 20150227 https://doi.org/10.1520/GTJ20150227.

Billi, A., Salvini, F., Storti, F., 2003. The damage zone-fault core transition in carbonate rocks: implications for fault growth, structure and permeability. J. Struct. Geol. 25, 1779–1794. https://doi.org/10.1016/ S0191-8141(03)00037-3.

Bourne, S.J., 2003. Contrast of elastic properties between rock layers as a mechanism for the initiation and orientation of tensile failure under uniform remote compression. J. Geophys. Res. 108, 2395. https://doi.org/ 10.1029/2001JB001725.

Caine, J.S., Evans, J.P., Forster, C.B., 1996. Fault zone architecture and permeability structure. Geology 24, 1025–1028.

Chester, F., Chester, J., Kirschner, D., Schulz, S., Evans, J., 2004. Structure of large- displacement, strike-slip fault zones in the brittle continental crust. Rheology and Deformation in the Lithosphere at Continental Margins 1, 223–260.

Childs, C., Manzocchi, T., Walsh, J.J., Bonson, C.G., Nicol, A., Scho¨pfer, M.P.J., 2009. A geometric model of fault zone and fault rock thickness variations. J. Struct. Geol. 31, 117–127. https://doi.org/10.1016/j.jsg.2008.08.009.

Childs, C., Worthington, R.P., Walsh, J.J., Roche, V., 2019. Conjugate relay zones: geometry of displacement transfer between opposed-dipping normal faults. J. Struct. Geol. 118, 377–390. https://doi.org/10.1016/j.jsg.2018.11.007.

Choi, J.-H., Edwards, P., Ko, K., Kim, Y.-S., 2016. Definition and classification of fault damage zones: a review and a new methodological approach. Earth Sci. Rev. 152, 70–87. https://doi.org/10.1016/j.earscirev.2015.11.006.

Cowie, P.A., Shipton, Z.K., 1998. Fault tip displacement gradients and process zone dimensions. J. Struct. Geol. 20, 983–997. https://doi.org/10.1016/S0191-8141(98) 00029-7.

Cowie, P.A., Sornette, D., Vanneste, C., 1995. Multifractal scaling properties of a growing fault population. Geophys. J. Int. 122, 457–469. https://doi.org/10.1111/j.1365- 246X.1995.tb07007.x.

Davy, P., Cobbold, P., 1991. Experiments on shortening of a 4-layer model of the continental lithosphere. Tectonophysics 188, 1–25.

de Joussineau, G., Mutlu, O., Aydin, A., Pollard, D.D., 2007. Characterization of strike- slip fault–splay relationships in sandstone. J. Struct. Geol. 29, 1831–1842. https:// doi.org/10.1016/j.jsg.2007.08.006.

Dresen, G., Gwildis, U., Kluegel, Th, 1991. Numerical and analogue modelling of normal fault geometry. Geological Society, London, Special Publications 56, 207–217. https://doi.org/10.1144/GSL.SP.1991.056.01.14.

Du Bernard, X., Labaume, P., Darcel, C., Davy, P., Bour, O., 2002. Cataclastic slip band distribution in normal fault damage zones, Nubian sandstones, Suez rift. J. Geophys. Res. Solid Earth 107. https://doi.org/10.1029/2001JB000493. ETG 6-1-ETG 6-12.

Evans, J.P., 1990. Thickness-displacement relationships for fault zones. J. Struct. Geol. 12, 1061–1065. https://doi.org/10.1016/0191-8141(90)90101-4.

Faulkner, D.R., Jackson, C.A.L., Lunn, R.J., Schlische, R.W., Shipton, Z.K., Wibberley, C. A.J., Withjack, M.O., 2010. A review of recent developments concerning the structure, mechanics and fluid flow properties of fault zones. J. Struct. Geol. 32, 1557–1575. https://doi.org/10.1016/j.jsg.2010.06.009.

Faulkner, D.R., Mitchell, T.M., Healy, D., Heap, M.J., 2006. Slip on “weak” faults by the rotation of regional stress in the fracture damage zone. Nature 444, 922–925. https://doi.org/10.1038/nature05353.

Ferrill, D.A., Morris, A.P., McGinnis, R.N., 2009. Crossing conjugate normal faults in field exposures and seismic data. AAPG (Am. Assoc. Pet. Geol.) Bull. 93, 1471–1488. https://doi.org/10.1306/06250909039.

Fossen, H., 2016. Structural Geology. Cambridge University Press. Goebel, T.H.W., Brodsky, E.E., 2018. The spatial footprint of injection wells in a global compilation of induced earthquake sequences. Science 361, 899–904. https://doi. org/10.1126/science.aat5449.

Gupta, A., Scholz, C.H., 2000. A model of normal fault interaction based on observations and theory p. J. Struct. Geol. 15.

Gupta, A., Scholz, C.H., 1998. Utility of elastic models in predicting fault displacement fields. J. Geophys. Res. Solid Earth 103, 823–834. https://doi.org/10.1029/ 97JB03009.

Hansberry, R.L., King, R.C., Holford, S.P., Hand, M., Debenham, N., 2021. How wide is a fault damage zone? Using network topology to examine how fault-damage zones overprint regional fracture networks. J. Struct. Geol. 146, 104327 https://doi.org/ 10.1016/j.jsg.2021.104327.

Heermance, R., Shipton, Z.K., Evans, J.P., 2003. Fault structure control on fault slip and ground motion during the 1999 rupture of the Chelungpu fault, Taiwan. Bull. Seismol. Soc. Am. 93, 1034–1050.

Hubbert, M.K., 1937. Theory of scale models as applied to the study of geologic structures. Bull. Geol. Soc. Am. 48, 1459–1520.

Illies, J.H., Greiner, G., 1979. Holocene movements and state of stress in the Rhinegraben rift system. Tectonophysics 52, 349–359.

Jackson, C.A.L., Gawthorpe, R.L., Sharp, I.R., 2006. Style and sequence of deformation during extensional fault-propagation folding: examples from the Hammam Faraun and El-Qaa fault blocks, Suez Rift, Egypt. J. Struct. Geol. 28, 519–535. https://doi. org/10.1016/j.jsg.2005.11.009.

Jackson, C.A.-L., Rotevatn, A., 2013. 3D seismic analysis of the structure and evolution of a salt-influenced normal fault zone: a test of competing fault growth models. J. Struct. Geol. 54, 215–234. https://doi.org/ 10.1016/j.jsg.2013.06.012.

Johansen, T.E.S., Fossen, H., 2008. Internal geometry of fault damage zones in interbedded siliciclastic sediments. Geological Society, London, Special Publications 299, 35–56. https://doi.org/10.1144/SP299.3.

Jorand, C., Chemenda, A.I., Petit, J.-P., 2012. Formation of parallel joint sets and shear band/fracture networks in physical models. Tectonophysics 581, 84–92. https://doi. org/10.1016/j.tecto.2011.11.021.

Karam, P., Mitra, S., Marfurt, K., Carpenter, B.M., 2021. Synthetic transfer zone characterization using seismic attributes: an example from the Parihaka fault system in the Taranaki Basin, New Zealand. Interpretation 9, T653–T665. https://doi.org/ 10.1190/INT-2020-0138.1.

Kim, Y.-S., Peacock, D.C.P., Sanderson, D.J., 2004. Fault damage zones. J. Struct. Geol. 26, 503–517. https://doi.org/10.1016/j.jsg.2003.08.002.

Kim, Y.-S., Peacock, D.C.P., Sanderson, D.J., 2003. Mesoscale strike-slip faults and damage zones at Marsalforn, Gozo Island, Malta. J. Struct. Geol. 25, 793–812. https://doi.org/10.1016/ S0191-8141(02)00200-6.

Knott, S.D., Beach, A., Brockbank, P.J., Brown, J.L., McCallum, J.E., Welbon, A.I., 1996. Spatial and mechanical controls on normal fault populations. J. Struct. Geol. 18, 359–372.

Liao, Z., Liu, H., Carpenter, B.M., Marfurt, K.J., Reches, Z., 2019. Analysis of fault damage zones using three-dimensional seismic coherence in the Anadarko Basin, Oklahoma. AAPG (Am. Assoc. Pet. Geol.) Bull. 103, 1771–1785. https://doi.org/ 10.1306/1219181413417207.

Maerten, L., Gillespie, P., Pollard, D.D., 2002. Effects of local stress perturbation on secondary fault development. J. Struct. Geol. 24, 145–153. https://doi.org/10.1016/ S0191-8141(01)00054-2.

Mansfield, C., Cartwright, J., 2001. Fault growth by linkage: observations and implications from analogue models. J. Struct. Geol. 23, 745–763. https://doi.org/ 10.1016/S0191-8141(00)00134-6.

Maqbool, A.-R., Moustafa, A.R., Dowidar, H., Yousef, M., 2016. Architecture of fault damage zones of normal faults, Gebel Ataqa area, Gulf of Suez rift, Egypt. Mar. Petrol. Geol. 77, 43–53. https://doi.org/ 10.1016/j.marpetgeo.2016.04.012.

Marchal, D., Guiraud, M., Rives, T., 2003. Geometric and morphologic evolution of normal fault planes and traces from 2D to 4D data. J. Struct. Geol. 25, 135–158. https://doi.org/10.1016/S0191-8141(02)00011-1.

Marchal, D., Guiraud, M., Rives, T., van den Driessche, J., 1998. Space and time propagation processes of normal faults. Geological Society, London, Special Publications 147, 51–70. https://doi.org/10.1144/GSL.SP. 1998.147.01.04.

Martinelli, M., Bistacchi, A., Mittempergher, S., Bonneau, F., Balsamo, F., Caumon, G., Meda, M., 2020. Damage zone characterization combining scan-line and scan-area analysis on a km-scale Digital Outcrop Model: the Qala Fault (Gozo). J. Struct. Geol. 140, 104144 https://doi.org/10.1016/j.jsg.2020.104144.

Mayolle, S., Soliva, R., Caniven, Y., Wibberley, C., Ballas, G., Milesi, G., Dominguez, S., 2019. Scaling of fault damage zones in carbonate rocks. J. Struct. Geol. 124, 35–50. https://doi.org/10.1016/j.jsg.2019.03.007.

Mayolle, S., Soliva, R., Dominguez, S., Wibberley, C., Caniven, Y., 2021. Nonlinear fault damage zone scaling revealed through analog modeling. Geology 49, 968–972. https://doi.org/10.1130/G48760.1.

McGrath, A.G., Davison, I., 1995. Damage zone geometry around fault tips. J. Struct. Geol. 17, 1011–1024.

Meixner, J., Schill, E., Gaucher, E., Kohl, T., 2014. Inferring the in situ stress regime in deep sediments: an example from the Bruchsal geothermal site. Geoth. Energy 2, 7. https://doi.org/10.1186/s40517-014-0007-z.

Meixner, J., Schill, E., Grimmer, J.C., Gaucher, E., Kohl, T., Klingler, P., 2016. Structural control of geothermal reservoirs in extensional tectonic settings: an example from the Upper Rhine Graben. J. Struct. Geol. 82, 1–15. https://doi.org/10.1016/j. jsg.2015.11.003.

Micarelli, L., Benedicto, A., Wibberley, C.A.J., 2006. Structural evolution and permeability of normal fault zones in highly porous carbonate rocks. J. Struct. Geol. 28, 1214–1227. https://doi.org/10.1016/j.jsg. 2006.03.036.

Micarelli, L., Moretti, I., Daniel, J.M., 2003. Structural properties of rift-related normal faults: the case study of the Gulf of Corinth, Greece. J. Geodyn. 36, 275–303. https:// doi.org/10.1016/S0264-3707(03)00051-6.

Milesi, G., Soliva, R., Moni´e, P., Münch, P., Bellanger, M., Bruguier, O., Bonno, M., Taillefer, A., Mayolle, S., 2019. Mapping a geothermal anomaly using apatite (U- Th)/He thermochronology in the Tˆet fault damage zone, eastern Pyrenees, France. Terra. Nova 31, 569–576. https://doi.org/10.1111/ter.12429.

Mitchell, T.M., Faulkner, D.R., 2009. The nature and origin of off-fault damage surrounding strike-slip fault zones with a wide range of displacements: a field study from the Atacama fault system, northern Chile. J. Struct. Geol. 31, 802–816. https:// doi.org/10.1016/j.jsg.2009.05.002.

Morley, C.K., 1995. Developments in the structural geology of rifts over the last decade and their impact on hydrocarbon exploration. Geological Society, London, Special Publications 80, 1–32. https://doi.org/ 10.1144/GSL.SP.1995.080.01.01.

Morley, C.K., Nelson, R.A., Patton, T.L., Munn, S.G., 1990. Transfer zones in the East african rift system and their relevance to hydrocarbon exploration in rifts (1). AAPG (Am. Assoc. Pet. Geol.) Bull. 74 https:// doi.org/10.1306/0C9B2475-1710-11D7- 8645000102C1865D.

Nicol, A., Walsh, J., Berryman, K., Nodder, S., 2005. Growth of a normal fault by the accumulation of slip over millions of years. J. Struct. Geol. 27, 327–342. https://doi. org/10.1016/j.jsg.2004.09.002.

Nicol, A., Walsh, J.J., Watterson, J., Bretan, P.G., 1995. Three-dimensional geometry and growth of conjugate normal faults. J. Struct. Geol. 17, 847–862. https://doi.org/ 10.1016/0191-8141(94)00109-D.

Ostermeijer, G.A., Aben, F.M., Mitchell, T.M., Rockwell, T.K., Rempe, M., Farrington, K., 2022. Evolution of co-seismic off-fault damage towards pulverisation. Earth Planet Sci. Lett. 579, 117353 https://doi.org/ 10.1016/j.epsl.2021.117353.

Ostermeijer, G.A., Mitchell, T.M., Aben, F.M., Dorsey, M.T., Browning, J., Rockwell, T.K., Fletcher, J.M., Ostermeijer, F., 2020. Damage zone heterogeneity on seismogenic faults in crystalline rock; a field study of the Borrego Fault, Baja California. J. Struct. Geol. 137, 104016 https://doi.org/10.1016/j.jsg.2020.104016.

Papamichos, E., Papanastasiou, P., Pasternak, E., Dyskin, A. (Eds.), 2017. Bifurcation and Degradation of Geomaterials with Engineering Applications: Proceedings of the 11th International Workshop on Bifurcation and Degradation in Geomaterials Dedicated to Hans Muhlhaus, Limassol, Cyprus, 21-25 May 2017. Springer Series in Geomechanics and Geoengineering. Springer International Publishing, Cham. https://doi.org/ 10.1007/978-3-319-56397-8.

Peacock, D.C.P., 2001. The temporal relationship between joints and faults. J. Struct. Geol. 23, 329–341. https://doi.org/10.1016/S0191-8141(00)00099-7.

Peacock, D.C.P., Dimmen, V., Rotevatn, A., Sanderson, D.J., 2017. A broader classification of damage zones. J. Struct. Geol. 102, 179–192. https://doi.org/ 10.1016/j.jsg.2017.08.004.

Peacock, D.C.P., Knipe, R.J., Sanderson, D.J., 2000. Glossary of normal faults. J. Struct. Geol. 22, 291–305. https://doi.org/10.1016/S0191-8141(00)80102-9.

Peacock, D.C.P., Sanderson, D.J., 1991. Displacements, segment linkage and relay ramps in normal fault zones. J. Struct. Geol. 13, 721–733.

Perrin, C., Manighetti, I., Gaudemer, Y., 2016. Off-fault tip splay networks: a genetic and generic property of faults indicative of their long-term propagation. Compt. Rendus Geosci. 348, 52–60. https://doi.org/10.1016/j.crte.2015.05.002.

Pollard, D.D., Aydin, A., 1988. Progress in understanding jointing over the past century. Geol. Soc. Am. Bull. 100, 1181–1204.

Reber, J.E., Cooke, M.L., Dooley, T.P., 2020. What model material to use? A Review on rock analogs for structural geology and tectonics. Earth Sci. Rev. 202, 103107 https://doi.org/10.1016/j.earscirev.2020.103107.

Rotevatn, A., Jackson, C.A.-L., Tvedt, A.B.M., Bell, R.E., Blækkan, I., 2019. How do normal faults grow? J. Struct. Geol. 125, 174–184. https://doi.org/10.1016/j. jsg.2018.08.005.

Sanderson, D.J., Peacock, D.C.P., 2019. Line sampling of fracture swarms and corridors. J. Struct. Geol. 122, 27–37. https://doi.org/10.1016/j.jsg.2019.02.006.

Savage, H.M., Brodsky, E.E., 2011. Collateral damage: evolution with displacement of fracture distribution and secondary fault strands in fault damage zones. J. Geophys. Res. 116 https://doi.org/10.1029/2010JB007665.

Schellart, W.P., 2002. Analogue modelling of large-scale tectonic processes: an introduction. J. Virtual Explor. 7 https://doi.org/10.3809/jvirtex.2002.00045.

Schlagenhauf, A., Manighetti, I., Malavieille, J., Dominguez, S., 2008. Incremental growth of normal faults: insights from a laser-equipped analog experiment. Earth Planet Sci. Lett. 273, 299–311. https://doi.org/10.1016/j.epsl.2008.06.042. Schlische, R.W., 1995. Geometry and origin of fault-related folds in extensional settings. AAPG (Am. Assoc. Pet. Geol.) Bull. 79, 1661–1678.

Schmittbuhl, J., Lambotte, S., Lenglin´e, O., Grunberg, M., Jund, H., Vergne, J.,

Cornet, F., Doubre, C., Masson, F., 2022. Induced and triggered seismicity below the city of strasbourg, France from november 2019 to january 2021. Comptes Rendus. Geoscience 353, 561–584. https://doi.org/10.5802/crgeos.71.

Schueller, S., Braathen, A., Fossen, H., Tveranger, J., 2013. Spatial distribution of deformation bands in damage zones of extensional faults in porous sandstones: statistical analysis of field data. J. Struct. Geol. 52, 148–162. https://doi.org/ 10.1016/j.jsg.2013.03.013.

Schulz, S.E., Evans, J.P., 2000. Mesoscopic structure of the Punchbowl Fault, Southern California and the geologic and geophysical structure of active strike-slip faults.
J. Struct. Geol. 22, 913–930.

Schwarz, B., Krawczyk, C.M., 2020. Coherent diffraction imaging for enhanced fault and fracture network characterization. Solid Earth 11, 1891–1907. https://doi.org/ 10.5194/se-11-1891-2020.

Segall, P., Pollard, D., 1980. Mechanics of discontinuous faults. J. Geophys. Res. Solid Earth 85, 4337–4350.

Shipton, Z.K., Cowie, P.A., 2001. Damage zone and slip-surface evolution over μm to km scales in high-porosity Navajo sandstone, Utah. J. Struct. Geol. 23, 1825–1844. Sibson, R.H., 2000. Fluid involvement in normal faulting. J. Geodyn. 29, 469–499.

Silva, M.E., Nogueira, F.C.C., P´erez, Y.A.R., Vasconcelos, D.L., Stohler, R.C., Sanglard, J. C.D., Balsamo, F., Bezerra, F.H.R., Carvalho, B.R.B.M., Souza, J.A.B., 2022. Permeability modeling of a basin-bounding fault damage zone in the Rio do Peixe Basin, Brazil. Mar. Petrol. Geol. 135, 105409 https://doi.org/10.1016/j. marpetgeo.2021.105409.

Soliva, R., Benedicto, A., 2004. A linkage criterion for segmented normal faults. J. Struct. Geol. 26, 2251–2267. https://doi.org/10.1016/j.jsg.2004.06.008.

Soliva, R., Benedicto, A., Schultz, R.A., Maerten, L., Micarelli, L., 2008. Displacement and interaction of normal fault segments branched at depth: implications for fault growth and potential earthquake rupture size. J. Struct. Geol. 30, 1288–1299. https://doi. org/10.1016/j.jsg.2008.07.005.

Solum, J.G., Huisman, B.A.H., 2017. Toward the creation of models to predict static and dynamic fault-seal potential in carbonates. Petrol. Geosci. 23, 70–91. https://doi. org/10.1144/petgeo2016-044.

Taillefer, A., Guillou-Frottier, L., Soliva, R., Magri, F., Lopez, S., Courrioux, G., Millot, R., Ladouche, B., Le Goff, E., 2018. Topographic and faults control of hydrothermal circulation along dormant faults in an orogen. G-cubed 19, 4972–4995.

Tapponier, P., Brace, W., 1976. Development of stress induced micro-cracks in Westerly granite. Int. J. Rock Mech. Min. Sci. 13.

Trice, R., Holdsworth, R., Rogers, S., McCaffrey, K., 2018. Characterising the fracture properties of lewisian Gneiss basement reservoirs, Rona ridge, west of shetland. In: The Geology of Fractured Reservoirs, 24–25 October, London. Programme and Abstract Volume 55.

Trippanera, D., Acocella, V., Ruch, J., Abebe, B., 2015. Fault and graben growth along active magmatic divergent plate boundaries in Iceland and Ethiopia: deformation at divergent boundaries. Tectonics 34, 2318–2348. https://doi.org/10.1002/ 2015TC003991.

Van Puymbroeck, N., Michel, R., Binet, R., Avouac, J.-P., Taboury, J., 2000. Measuring earthquakes from optical satellite images. Appl. Opt. 39, 3486. https://doi.org/ 10.1364/AO.39.003486.

Visage, S., Souloumiac, P., Cubas, N., Maillot, B., Antoine, S., Delorme, A., Klinger, Y., 2023. Evolution of the off-fault deformation of strike-slip faults in a sand-box experiment. Tectonophysics 847, 229704. https://doi.org/10.1016/j. tecto.2023.229704.

Walsh, J.J., Nicol, A., Childs, C., 2002. An alternative model for the growth of faults. J. Struct. Geol. 24, 1669–1675. https://doi.org/10.1016/S0191-8141(01)00165-1.

Watterson, J., Nicol, A., Walsh, J.J., Meier, D., 1998. Strains at the intersections of synchronous conjugate normal faults. J. Struct. Geol. 20, 363–370. https://doi.org/ 10.1016/S0191-8141(97)00100-4.

Wessel, P., Smith, W.H.F., Scharroo, R., Luis, J., Wobbe, F., 2013. Generic mapping tools: improved version released. Eos, Transactions American Geophysical Union 94, 409–410. https://doi.org/ 10.1002/2013EO450001.

Wibberley, C.A.J., Gonzalez-Dunia, J., Billon, O., 2017. Faults as barriers or channels to production-related flow: insights from case studies. Petrol. Geosci. 23, 134–147. https://doi.org/10.1144/petgeo2016-057.

Wibberley, C.A.J., Petit, J.-P., Rives, T., 2000. Micromechanics of shear rupture and the control of normal stress. J. Struct. Geol. 22, 411–427. https://doi.org/10.1016/ S0191-8141(99)00158-3.

Withjack, M.O., Schlische, R.W., Olsen, P.E., 2002. Rift-basin Structure and its Influence on Sedimentary Systems.

Zwaan, F., Schreurs, G., Madritsch, H., Herwegh, M., 2022. Influence of rheologically weak layers on fault architecture: insights from analogue models in the context of the Northern Alpine Foreland Basin. Swiss J. Geosci. 115, 26. https://doi.org/ 10.1186/s00015-022-00427-8.